Draft version September 9, 2026
Typeset using LaTeX default style in AASTeX631

arXiv:2609.08604v1 [astro-ph.IM] 8 Sep 2026

A Missing Tool for Calculating Auto/Cross-correlation Function under Nonuniform Sampling Observations

Chen-Ran Hu (胡宸然) [1], Yong-Feng Huang (黄永锋) [1,2,*], Jin-Jun Geng (耿金军) [3], Orkash Amat (吾热卡西 · 艾麦提) [1], Ze-Cheng Zou (邹泽城) [1], Chen Deng (邓晨) [1], Fan Xu (许帆) [4], Xiao-Fei Dong (董小飞) [1], Chen Du (杜琛) [1], Nurimangul Nurmamat (努尔曼古丽 · 努尔麦麦提) [5], Pei Wang (王培) [6,7], Lang Cui (崔朗) [8,9] and Cheng-Ming Li (李程明) [10]

[1] School of Astronomy and Space Science, Nanjing University, Nanjing 210023, China
[2] Key Laboratory of Modern Astronomy and Astrophysics (Nanjing University), Ministry of Education, China
[3] Purple Mountain Observatory, Chinese Academy of Sciences, Nanjing 210023, China
[4] Institute of Space Weather, School of Atmospheric Physics, Nanjing University of Information Science and Technology, Nanjing 210044, China
[5] Guangxi Key Laboratory for Relativistic Astrophysics, School of Physical Science and Technology, Guangxi University, Nanning 530004, China
[6] State Key Laboratory of Radio Astronomy and Technology, NAOC, Chinese Academy of Sciences, Beijing 100101, China
[7] Institute for Frontiers in Astronomy and Astrophysics, Beijing Normal University, Beijing 102206, China
[8] State Key Laboratory of Radio Astronomy and Technology, Xinjiang Astronomical Observatory, CAS, 150 Science 1-Street, Urumqi, Xinjiang, 830011, China
[9] Xinjiang Key Laboratory of Radio Astrophysics, 150 Science 1-Street, Urumqi 830011, China
[10] Institute for Astrophysics, School of Physics, Zhengzhou University, Zhengzhou 450001, China

ABSTRACT

Nonuniform sampling presents a long-standing challenge in astrophysical time-domain analysis, invalidating the standard autocorrelation and cross-correlation functions and forcing researchers to adopt ad-hoc methods like interpolation or binning, which introduce unquantified biases and lack rigorous error estimation. Here we introduce a new method for calculating the nonuniform autocorrelation function (NUACF) and nonuniform cross-correlation function (NUCCF) for irregularly sampled time series. Instead of relying on interpolation, it naturally evaluates the correlation function by incorporating time-interval weights and misalignment penalties. Monte Carlo simulations provide confidence bands for significance assessment and a complete error budget for the time delays that accounts for both flux uncertainties and sampling irregularity (essential but generally absent from existing methods). Through extensive simulations, we demonstrate that our method outperforms traditional methods across various conditions, from strictly periodic to complex repeating variability patterns (e.g., intermittent but aperiodic). Its effectiveness is demonstrated via various real astrophysical data sets, revealing repetitive variability in stellar light curves, measuring time delays for multi-band disc reverberation in the AGN Fairall 9, and providing model-independent validation of time delays for the gravitationally lensed quasar HE 0435-1223. The method provides a rigorous and general solution to the ubiquitous problem of nonuniform sampling, positioning it as a useful tool for large-scale time-domain survey data analysis. The framework is also directly applicable to emerging time-domain phenomena such as fast radio bursts (FRBs), enabling, for example, the study of correlations between persistent radio source luminosity and repeating FRB activity, or among the multi-parameter variability curves of FRB emission itself.

Keywords: Time series analysis (1916); Irregular cadence (1953); Time domain astronomy (2109); Theoretical techniques (2093); Active galactic nuclei(16); Gravitational lensing (670); Variable stars (1761); Radio transient sources (2008)

1. INTRODUCTION

Autocorrelation function (ACF) and cross-correlation function (CCF) are useful mathematical tools for quantifying repetitive structures of a timing series or the connection between two timing series. Their core concept of measuring similarity permeates various branches of astrophysics, finding applications across the temporal, spatial, and frequency domains.

For continuous functions or uniformly sampled timing series, ACF/CCF can be conveniently calculated. Classic applications include characterizing the variability timescales of active galactic nuclei (AGN) (Kelly et al. 2009), describing charged-particle motion in turbulent magnetic fields relevant to cosmic-ray propagation (Jokipii 1966), formulating analytical models for the gravitational clustering of dark matter halos (Mo & White 1996), developing a framework for analyzing full-sky cosmic microwave background temperature and polarization maps (Kamionkowski et al. 1997), and employing the two-point correlation function to describe the distribution of cosmic matter (Peebles 1980; Davis & Peebles 1983; Landy & Szalay 1993; Kauffmann et al. 1999; Springel et al. 2018). Furthermore, since the power spectral density and the ACF form a Fourier transform pair (the Wiener-Khinchin theorem), theoretical studies of the power spectrum can be viewed as equivalently specifying a particular form of ACF. Examples encompass modeling AGN X-ray variability driven by thermal fluctuations in accretion disks (Lyubarskii 1997) and outlining a method to generate time series with power-law power spectrum (Timmer & König 1995).

When applied to observational data, ACF/CCF are usually calculated by introducing an additional normalization factor to get the normalized correlation function. Representative applications cover diverse tasks such as measuring stellar variability periods (McQuillan et al. 2013), disentangling various stellar oscillation modes in asteroseismology (Mosser & Appourchaux 2009), analyzing long-term periodicity in fast radio bursts (FRBs) (Pal 2025), combining with classical reverberation mapping to constrain AGN broad-line region sizes and central black hole masses (Peterson et al. 2004; Pancoast et al. 2014) and with intensive disc-reverberation mapping to probe AGN accretion disk structures (Pal et al. 2017; Hernández Santisteban et al. 2020a), determining spatial scales of the solar wind (King & Papitashvili 2005), measuring baryon acoustic oscillations in survey data via the two-point correlation function (Eisenstein et al. 2005; Beutler et al. 2011; du Mas des Bourboux et al. 2017), and constraining the sizes of FRB emission regions based on spectral lags (Nimmo et al. 2025).

In practice, astronomical observations are usually performed through nonuniform sampling, which poses a major challenge to the correlation analysis, with the exception of frequency-domain measurements such as spectral lags [e.g., Nimmo et al. (2025)]. This renders the normal methods involving uniformly sampled ACF/CCF inapplicable, forcing researchers to seek adaptive methods. In spatial-domain applications involving the two-point correlation function, nonuniformity often arises from finite sky coverage due to Galactic avoidance, field tiling, or cosmic extinction. The established remedy is the Landy-Szalay estimator (Landy & Szalay 1993), which effectively eliminates systematic biases introduced by finite survey geometry.

Throughout this work, we focus on the normalized ACF and CCF, the forms yielding correlation coefficients in the range $[-1, 1]$, as these are the quantities typically used for statistical analysis such as temporal correlation and feature extraction. This is quite distinct from the unnormalized versions commonly employed in data processing and theoretical astrophysics, which differ by a normalization term. We emphasize that such time-domain correlation

* Email: hyf@nju.edu.cn

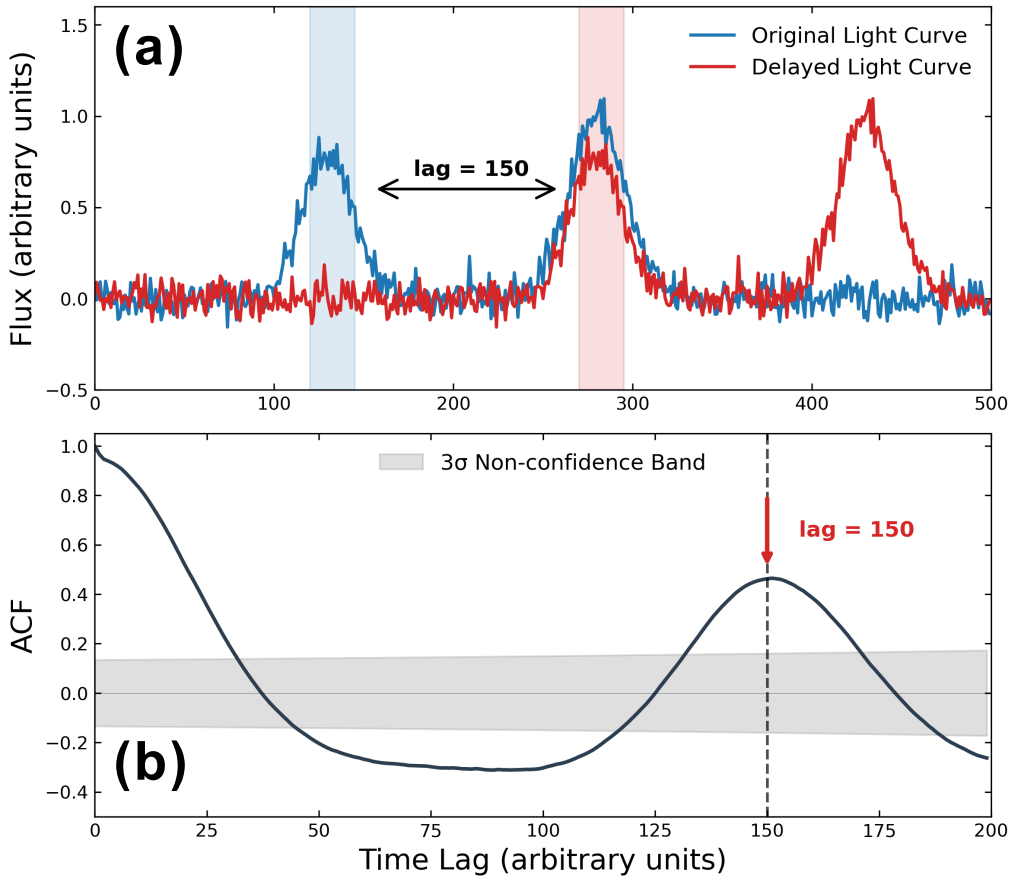


Figure 1. Schematic illustration of the standard ACF procedure under uniform sampling. (a) A light curve (blue), which exhibits repeating variability patterns, is shifted by a trial time delay to become the shifted copy (red). (b) Repeating this procedure over a range of trial time delays yields the ACF profile. The horizontal gray region indicates the 3σ non-confidence band, meaning that an ACF value falling within this band has a 99.73% probability of arising from random statistical fluctuations of the data points. By convention, however, this region is still commonly referred to as the "confidence band". A significant peak above this band indicates the recurrence timescale of the variability.

analysis is significantly different from frequency-domain methods such as the Fourier transform or the Lomb-Scargle periodogram (Lomb 1976; Scargle 1982; VanderPlas 2018), which aim to identify periodicities rather than directly characterize repeating temporal patterns (including intermittent, aperiodic ones).

The core idea of the normalized ACF is sketched in Figure 1(a): one shifts a light curve by a trial time delay, computes how well it matches itself, and obtains a single correlation coefficient. Repeating this over a range of trial time delays yields the ACF profile as shown in Figure 1(b). A significant peak (one that rises above the confidence band) then indicates the timescale of the repeating patterns in the light curve. The normalized CCF shares the same logic, but compares two different light curves. We note that Figure 1 illustrates the standard ACF procedure under uniform sampling, where a well-defined confidence band is readily available. However, in the case of nonuniform sampling, such a band is generally unavailable, which leads to difficulty in the ACF/CCF analysis.

Temporal sampling irregularity, stemming from factors such as source visibility, Earth rotation and orbit motion, instrumental maintenance, and observing schedule competition, constitutes an impediment distinct from the geometric effects in spatial sampling. Traditional approaches often rely on interpolating or resampling the unevenly sampled time series (Sun et al. 2018) or binning time delays, as adopted in the discrete correlation function (DCF) method

(Edelson & Krolik 1988). While these methods mitigate issues from irregular sampling, they introduce additional, usually unquantified artificial biases, leading to three key shortcomings:

(1) Lack of confidence estimation. Standard sample ACF/CCF for uniform data provides confidence intervals, allowing one to distinguish genuine peaks and troughs from noise. Interpolated/resampled ACFs typically lack this, reducing their utility to mere period detection (via equally spaced peaks/troughs) and impairing the identification of aperiodic recurring patterns and their delays. Similarly, while DCF can indicate a delay at a peak, it offers no direct statistical assessment of the peak's validity.

(2) Inability to assess the significance of identified recurring patterns. Closely related to the first point, the absence of confidence intervals precludes a robust significance evaluation for potential recurring patterns associated with ACF/CCF features.

(3) Incomplete error estimation for time-delay measurements. A complete error budget for a time delay should incorporate both flux measurement uncertainties and the effects of sampling irregularity. In traditional approaches, Monte Carlo (MC) simulations are typically introduced to handle the former but do not capture the latter. Specifically, interpolation/resampling effectively removes the sampling-induced error but replaces it with an artificial, nonanalytic error that cannot be propagated rigorously. In the case of the DCF, the binning procedure also introduces artificial biases. The empirically chosen bin width trades temporal resolution for robustness: narrower bins increase resolution but reduce the number of matched pairs per bin. The DCF results thus depend on the bin width, because binning compresses the scatter of time delays within each bin into a single value (an inherently approximative step). This prevents the DCF from being fully analytic and hinders a complete uncertainty estimate, despite partially absorbing the effects of sampling irregularity.

Some existing approaches seek to mitigate artifacts in correlation analyses under irregular sampling, for instance, through conservative interpolation schemes such as zero padding or via data selection methods like the S-ACF (Kreutzer et al. 2023). While these ideas offer valuable insights, they remain non-analytic or semi-analytic in nature and therefore cannot fully resolve the problems outlined above (Press et al. 1992; Alexander 1997).

It is noteworthy that the seminal work of Franks (1981) derived the theoretical ACF for an ideal Poisson sampling process. This formalism was applied by Yang & Zhang (2023) to model the propagation of FRBs in the magnetosphere, assuming a coherent curvature radiation mechanism. While this is viable for theoretical modeling, it is generally unsuitable for inverse feature extraction from observations because real observational sampling patterns often deviate significantly from the Poisson assumption due to limited observing schedules and other artificial factors.

Consequently, a unified, analytical, tractable and model-agnostic framework for correlation analysis of nonuniform sampling remains lacking. This work aims to fill this gap by introducing a generalized, analytical ACF/CCF method that is applicable to nonuniformly sampled observations, providing confidence intervals, significance assessments, and a complete error budget for timing series. It degenerates to conventional ACF/CCF under uniform sampling. This approach thus offers a more direct and statistically rigorous tool for astrophysicists.

In Section 2, we present the derivation of the Nonuniform ACF (NUACF), detailing the method for determining its confidence intervals and the error budget for time-delay measurements. Section 3 extends this framework to the Nonuniform CCF (NUCCF). Section 4 demonstrates the practical application of both the NUACF and NUCCF to real astrophysical scenarios.

2. NONUNIFORM AUTOCORRELATION FUNCTION

Our derivation of the NUACF follows a generalizable principle: to extend estimators from the uniform to the nonuniform domain by replacing simple averages with time-weighted averages. This is most intuitively illustrated with the simpler case of variance. For a continuous time series $x(t)$, the variance over a duration T is $\sigma_{\mathrm{C}}^2 = \frac{1}{T}\int_0^T \left[x(t) - \overline{x(t)}\right]^2 \mathrm{d}t$. Discretizing this for observations $\{(x_i, t_i) | \, i = 1, 2, \cdots, N\}$ naturally leads to a time-

weighted estimator: $\sigma_{\mathrm{D}}^2 = \frac{1}{t_N - t_1} \sum_{i=1}^{N} (x_i - \bar{x})^2 \Delta t_i$. For uniformly sampled data, where all time intervals are equal ($\Delta t_i \equiv \Delta t$, implying $t_N - t_1 = (N-1)\Delta t$), this reduces to the standard sample variance. For nonuniform sampling, applying a numerical quadrature rule (e.g., the trapezoidal rule) provides a robust nonuniform variance estimator, $\sigma_{\mathrm{D,NU}}^2$. This transition from an integral to a time-weighted discrete sum forms the foundational template for generalizing the ACF. When applied to a uniform data set, we get the uniform sample ACF, $\mathrm{acf}_{\mathrm{D,U}}(k)$.

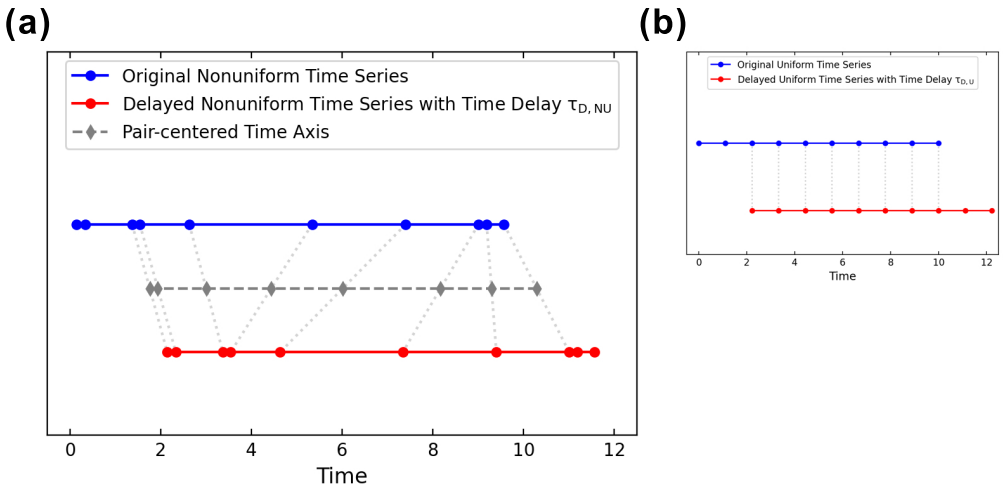


Figure 2. Temporal misalignment in nonuniform autocorrelation. (a) A nonuniformly sampled time series is illustrated. The blue dots mark the original observation times. Shifting the sequence by a lag of k data points produces the red series, whose time stamps do not align with the original ones. To compare these misaligned pairs (linked by gray dotted lines), a pair-centered time axis (gray dashed line) is constructed, defined as the midpoint between the two times in each matched pair. This axis is a virtual computational device solely for locating each pair in time and is algebraically eliminated in the final estimator (see Appendix A). (b) For comparison, under uniform sampling, the k-lag delayed series (red) can always align perfectly with the original one (blue) in the time domain, yielding a fixed trial time delay $k\Delta t$ and requiring no pair-centered time axis or misalignment penalty.

For nonuniform sampling, a shift by k indices does not temporally align data pairs (Figure 2). The NUACF framework addresses this by introducing a pair-centered time axis as a derivation device and solving two linked problems: (i) defining an optimal trial time delay $\tau_{\mathrm{D,NU}}(k)$ that minimizes the overall temporal misalignment for a given trial index lag k, and (ii) formulating a correlation measure that incorporates both time-interval weights and a penalty for temporal misalignment (Appendix A).

The optimal trial time delay is defined as the average temporal separation for the corresponding k-th lag:

$$\tau_{\mathrm{D,NU}}(k) = \frac{1}{N-k} \sum_{i=1}^{N-k} h_{i+k,i}, \tag{1}$$

where $h_{m,n} = t_m - t_n$. This ensures $\tau_{\mathrm{D,NU}}(k)$ reduces to $k\Delta t$ under uniform sampling and minimizes the expected residual misalignment to zero (Appendix A).

The correlation measure is then calculated by applying the time-weighted averaging principle to both the numerator and denominator of the dimensionless sample ACF. The local sampling density is incorporated via discrete weight factors $H_i^{(1)}$ and $H_i^{(2)}$ derived from the trapezoidal rule, while a Gaussian kernel weight w_i penalizes residual misalignment within each pair. This leads to the compact, final form of the NUACF:

$$\mathrm{acf}_{\mathrm{D,NU}}(k) = \frac{h_{N,1}}{h_{N-k,1} + h_{N,k+1}} \frac{\sum_{i=1}^{N-k} (x_i - \bar{x})(x_{i+k} - \bar{x}) H_i^{(2)} w_i}{\sum_{i=1}^{N} (x_i - \bar{x})^2 H_i^{(1)}}, \quad k \in \mathbb{N}, k \leq N - 10. \tag{2}$$

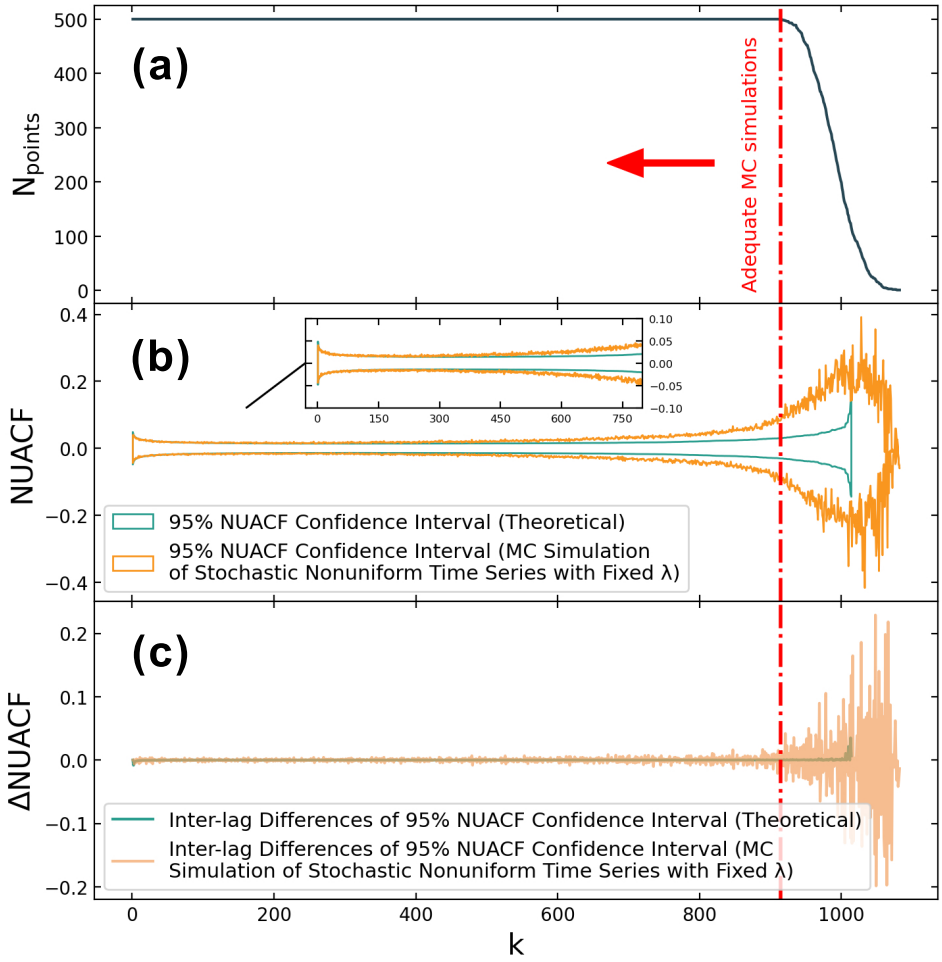


Figure 3. Validation of the theoretical nonuniform autocorrelation function (NUACF) confidence interval under ideal Poisson sampling. (a) Number of available data points (N_{points}) used to calculate the Monte Carlo (MC) confidence interval as a function of lag k. The vertical red dash-dotted line marks the lag beyond which N_{points} falls below the total number of simulations (500); only the region to its left is considered meaningful for estimation. (b) Comparison of the theoretical 95% confidence interval [solid green line, from Equation (3)] with that derived from 500 MC simulations (solid orange line) where both observation times and fluxes were randomly generated following a Poisson process. The two intervals agree well within a reliable lag range. (c) Differences of the upper confidence bounds, shown for both the theoretical (green) and MC (orange) cases. The discrepancy of the simulated confidence interval increases with k, which is due to fewer matched pairs. The NUACF loses its effectiveness beyond the reliable range.

The detailed definitions of $H_i^{(1)}$, $H_i^{(2)}$ and w_i are provided in Appendix A. This formulation is self-consistent and degenerates exactly to the standard sample ACF under uniform sampling.

To assess whether a peak in the NUACF signifies a real correlation, we require confidence intervals under the null hypothesis of white noise. For uniformly sampled data, this leads to the standard confidence estimation of $\pm z_{\alpha/2}/\sqrt{N-k}$. Extending this analytically to nonuniform sampling is complex. Under the assumption that the data points are sampled following a Poisson process, a theoretical NUACF confidence interval can be derived (see Appendix B for the complete derivation) as

$$\text{acf}_{\text{D,NU}}^{\text{noise}}(k) \in \left[-z_{\alpha/2}V(k), z_{\alpha/2}V(k)\right], \tag{3}$$

where $V(k)$ is a function of the lag k, the observed timestamps $\{t_i\}$, and the data variances.

Figure 3 compares the theoretical NUACF confidence interval with that obtained via MC simulations using white-noise sequences. In the MC case, for a given event rate λ, Poisson sampling is applied to randomly generate observation times and flux values in each simulation, yielding a white-noise series. The NUACF values at all lags k are recorded in the simulation. After completing all runs, the NUACF values at each k follow a normal distribution, from which the $100\,(1-\alpha)\,\%$ confidence interval is directly extracted to get the MC-based confidence estimation. A total of 500 simulations were conducted, providing 500 NUACF values at each k. However, due to Poisson sampling, the sample size differs across different simulations even under the same λ, leading to variation in the maximum computable k in each run. As shown in Figure 3(a), the number of available data points ($N_{\rm points}$) for constructing the MC confidence interval decreases as k increases. To ensure reliability, we consider a range of k as adequate where $N_{\rm points}$ remains equal to the total number of simulations (500), indicated by the vertical dash-dotted line at the left side.

Figure 3(b) demonstrates that within this effective range, the theoretical NUACF confidence interval given by Equation (3) agrees well with the MC-derived interval. Although minor deviations emerge at larger k, they still remain small enough (about 0.05 at most). These deviations originate from the finite number of simulations because, as k grows, the number of matched pairs available for NUACF computation decreases, reducing the robustness of the estimated NUACF [Equation (B12) in Appendix B] and thus causing the MC confidence interval to gradually depart from the theoretical one. In principle, such a deviation would be nonexistent for an infinite sample size case.

Figure 3(c) displays the inter-lag backward differences of the upper confidence bounds (the lower bounds behave symmetrically), comparing the theoretical and simulated cases. The discrepancy increases with k, confirming the aforementioned decrease in matched-pair counts. To the right of the vertical red dash-dotted line, the instability rises sharply.

At first glance, the theoretical NUACF confidence interval provided by Equation (3) appears to provide a good fit to the simulations in Figure 3. However, it is crucial to note that the simulations in Figure 3 randomly vary with both observation times and fluxes. In real observations, the sampling timestamps are actually fixed. Therefore, for an actual time series, the observation times cannot be randomized, and the theoretical interval will not perfectly match an MC interval constructed with fixed times. To clarify this point, a second type of simulation was performed, where observation times were fixed across runs while the flux values were randomized following a white-noise process. Figure 4 presents nine sets of such simulations, each set corresponding to a distinct fixed time series. While the theoretical interval generally captures the overall trend, it does not align closely with the MC interval, a behavior that persists regardless of the number of sampling points. Thus, although the theoretical confidence interval derived under ideal Poisson sampling is theoretically sound (Figure 3), it is less practical than an MC interval constructed with fixed observation times, because real observational times are fixed and thus not fully amenable to analytic modeling. Consequently, we suggest that confidence intervals for NUACF should be derived via MC simulation, which is adopted in all our calculations below.

When a significant NUACF peak is identified, determining the corresponding time delay $\tau_{\rm D,NU}$ with a definite uncertainty is useful. Two factors may contribute to the uncertainty: one is the inherent irregularity of the sampling times, and the other is the flux measurement error.

The uncertainty due to temporal irregularity can be derived from the dispersion of the pairwise time differences used in Equation (1):

$$\varepsilon_t\left[\tau_{\rm D,NU}\left(k\right)\right]=\frac{1}{N-k}\sqrt{\sum_{i=1}^{N-k}\left(h_{i+k,i}-\overline{h_{i+k,i}}\right)^2}. \tag{4}$$

The flux error contribution can be assessed via MC simulations, where fluxes are randomly perturbed within their measurement uncertainties. For a significant peak P_φ, once all MC runs are completed, the time delay of $\left\{\tau_{\rm D,NU}^{(\xi)}\left(k_{\mathrm{P}_\varphi}\right)\middle|\,\xi=1,2,\cdots,S\right\}$ and the corresponding temporal irregularity errors $\left\{\varepsilon_t\left[\tau_{\rm D,NU}^{(\xi)}\left(k_{\mathrm{P}_\varphi}\right)\right]\middle|\,\xi=1,2,\cdots,S\right\}$

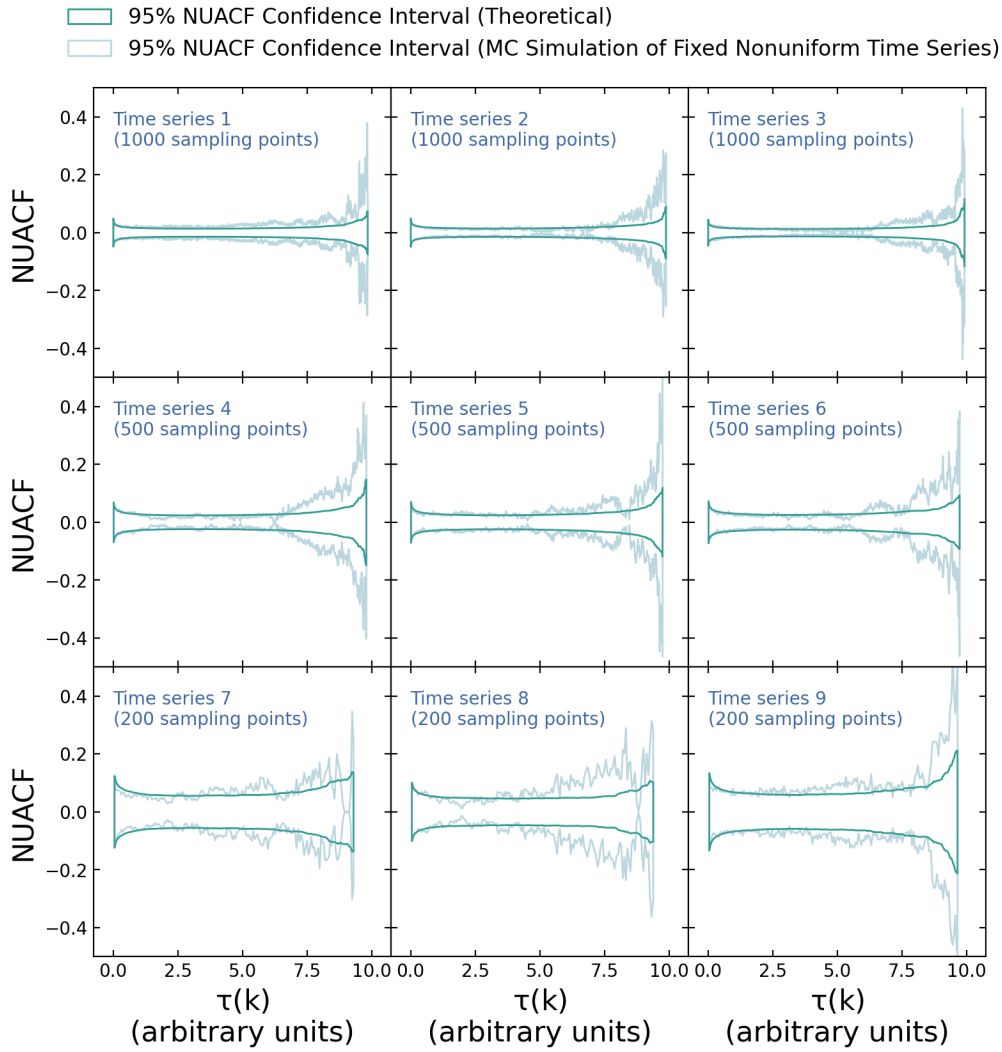


Figure 4. Limitation of the theoretical confidence interval for fixed observational timestamps. Nine independent sets of simulations are shown, where the observation times are fixed and only the flux values are randomized as white noise in each MC realization. In each panel, the solid green line shows the theoretical interval [Equation (3)], and the solid blue line shows the MC case constructed from 500 realizations. While the theoretical interval follows the general trend, it does not capture the detailed, structured deviations of the MC interval, which is a persistent discrepancy regardless of the number of sampling points. It demonstrates that a confidence interval derived from fixed-time MC simulations is more reliable than the purely analytic result derived under a Poisson-sampling assumption.

can be obtained. The final total uncertainty synthesizes the contributions from the two factors, which reads (Appendix C)

$$\varepsilon_{\text{total}}\left[\tau_{\text{D,NU}}\left(k_{\text{P}_\varphi}\right)\right]=\sqrt{\frac{\sum_{\xi}\left[\tau_{\text{D,NU}}^{(\xi)}\left(k_{\text{P}_\varphi}\right)-\overline{\tau_{\text{D,NU}}^{(\xi)}\left(k_{\text{P}_\varphi}\right)}\right]^2}{S\left(S-1\right)}+\overline{\left\{\varepsilon_t\left[\tau_{\text{D,NU}}^{(\xi)}\left(k_{\text{P}_\varphi}\right)\right]\right\}^2}}, \tag{5}$$

where $\overline{\tau_{\text{D,NU}}^{(\xi)}\left(k_{\text{P}_\varphi}\right)}$ is the final mean time delay (the ensemble mean). The first term in the above Equation corresponds to the standard error of the mean from the MC realizations, and the second corresponds to the root-mean-square temporal irregularity error.

To conclude, our NUACF provides a model-independent framework for autocorrelation analysis of irregularly sampled time series. It delivers a well-defined time delay and correlation measure, along with a robust estimate of the significance level and a useful uncertainty for the time delay.

3. NONUNIFORM CROSS-CORRELATION FUNCTION

We generalize the NUACF framework to calculate the CCF of two irregularly sampled time series, $\{(x_i, t_i^x)|\, i = 1, 2, \cdots, N\}$ and $\{(y_i, t_i^y)|\, i = 1, 2, \cdots, M\}$, which presents a useful method for nonuniform cross-correlation function (NUCCF) analysis. It provides a model-independent estimate of both the correlation measure and the time delay $\tau_{\mathrm{D,NU}}^{xy}(k)$ between the two series,

$$\mathrm{ccf}_{\mathrm{D,NU}}(k) = \frac{\sqrt{h_{N,1}^x h_{M,1}^y}}{h_{i_{\max},i_{\min}}^x + h_{i_{\max}+k,i_{\min}+k}^y} \frac{\sum_{i=i_{\min}}^{i_{\max}} (x_i - \bar{x})(y_{i+k} - \bar{y}) H_i^{xy,(2)} w_i^{xy}}{\sqrt{\sum_{i=1}^{N} (x_i - \bar{x})^2 H_i^{x,(1)} \sum_{i=1}^{M} (y_i - \bar{y})^2 H_i^{y,(1)}}}, \quad k \in \mathbb{Z}, -(N-10) \le k \le M-10, \tag{6}$$

where $i_{\min} = \max(1, 1-k)$, $i_{\max} = \min(N, M-k)$, $h_{m,n}^x = t_m^x - t_n^x$ and $h_{m,n}^y = t_m^y - t_n^y$. The discrete weight factors $H_i^{x,(1)}$, $H_i^{y,(1)}$, and $H_i^{xy,(2)}$, derived via the trapezoidal rule, and the misalignment weight w_i^{xy} (see Appendix D for definitions) can effectively correct for nonuniform sampling and temporal misalignment. The associated time delay at lag k is the mean temporal offset,

$$\tau_{\mathrm{D,NU}}^{xy}(k) = \overline{t_{i+k}^y - t_i^x} = \frac{1}{i_{\max} - i_{\min} + 1} \sum_{i=i_{\min}}^{i_{\max}} \left(t_{i+k}^y - t_i^x\right). \tag{7}$$

Similar to NUACF, significance of NUCCF is also assessed via MC confidence interval, and the final uncertainty synthesizes flux-error and nonuniform-sampling contributions. Note that for the two series, we construct a conservative, envelope-based confidence interval from two complementary MC procedures (fixing one series and replacing the other with a white noise series, then vice versa). The final uncertainty for a significant delay is:

$$\varepsilon_{\mathrm{total}}\left[\tau_{\mathrm{D,NU}}^{xy}(k)\right] = \sqrt{\frac{\sum_{\xi}\left[\tau_{\mathrm{D,NU}}^{xy,(\xi)}\left(k_{\mathrm{P}_\varphi}\right) - \overline{\tau_{\mathrm{D,NU}}^{xy,(\xi)}\left(k_{\mathrm{P}_\varphi}\right)}\right]^2}{S(S-1)} + \overline{\left\{\varepsilon_t\left[\tau_{\mathrm{D,NU}}^{xy,(\xi)}\left(k_{\mathrm{P}_\varphi}\right)\right]\right\}^2}}, \tag{8}$$

where the temporal irregularity error is

$$\varepsilon_t\left[\tau_{\mathrm{D,NU}}^{xy}(k)\right] = \sqrt{\frac{\sum_{i=i_{\min}}^{i_{\max}}\left(t_{i+k}^y - t_i^x - \overline{t_{i+k}^y - t_i^x}\right)^2}{(i_{\max} - i_{\min} + 1)(i_{\max} - i_{\min})}}. \tag{9}$$

Our NUCCF framework provides a useful cross-correlation tool for analyzing multi-instrument, multi-epoch astronomical data.

4. VALIDATION AND APPLICATION IN ASTRONOMICAL OBSERVATIONS

As the fist step, we have conducted a series of exhaustive simulation tests to evaluate the performance of our NUACF and NUCCF methods systematically. We first generated three different synthetic signals exhibiting repetitive variability patterns (e.g., simple periodic signals) along with injected noise. They are sampled under both quasi-uniform (Figures 5.1–5.3) and nonuniform (Figures 5.4–5.6) schemes. We then analyzed these signals using the resampled ACF (which reconstructs a uniformly sampled series by assigning the flux value of the temporally nearest observation to each grid point, thus generating no new data), the interpolated ACF, and our NUACF method. The results demonstrate that the resampled ACF, the first-order interpolated ACF, and the NUACF can all successfully identify the time delays

corresponding to the repetitive patterns. Note that our NUACF assesses the significance not by its curve morphology but by considering whether the peaks/troughs lie outside the corresponding confidence interval. We also notice that for a fixed total time span, a higher sampling density yields lower absolute NUACF values, but the confidence interval also narrows accordingly, thus its ability to identify significant features is not affected.

Fig. Set 5. Systematic simulation tests for NUACF performance under diverse sampling and windowing conditions

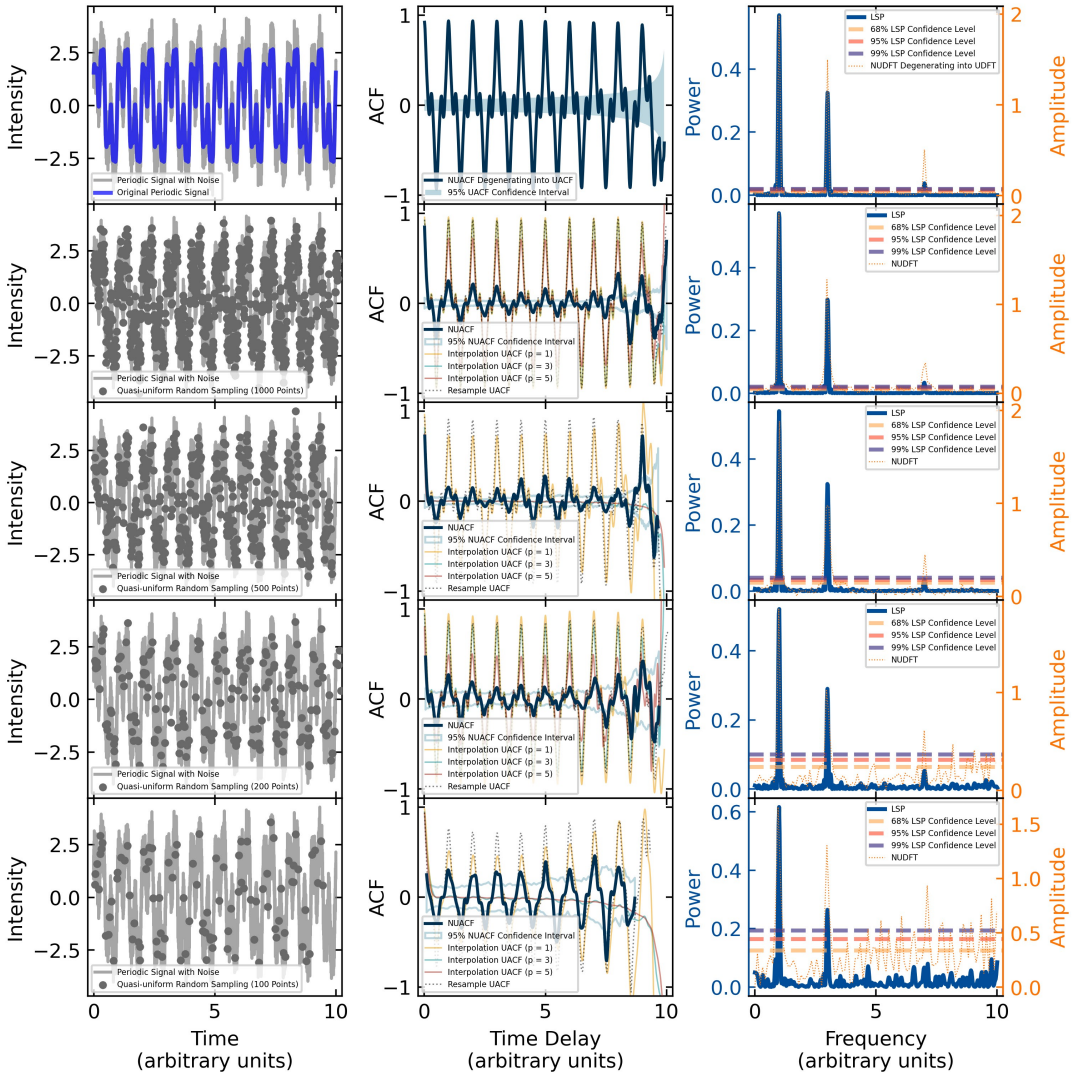


Figure 5. Exemplary synthetic signal (Pattern A) under quasi uniform sampling. The complete figure set (18 images) is available in the online journal. For the first image, the description is: Shown here is the ACF analysis of a quasi uniformly sampled periodic signal with noise added, designated as Pattern A. Left column: The input periodic signal, shown from densely uniform sampling (top) to progressively sparser quasi-uniform sampling. Middle column: ACF analysis of the corresponding signals to the left. The NUACF (dark blue line, with the 95% confidence interval shown as the blue region), resampled ACF (dotted gray line), and interpolated ACF of orders $p = 1, 3, 5$ (orange, green, red) are shown. The top panel demonstrates that the NUACF reduces exactly to the standard sample ACF under uniform sampling. Right column: Power spectra of the signals to the left, from LSP (blue solid line, left axis) and a nonuniform discrete Fourier transform (NUDFT, orange dotted line, right axis) implemented via the trapezoidal rule. [The complete figure set (18 images) is available in the online journal.]

Fig. Set 6. Robustness comparison between resampled ACF and NUACF under complex signal conditions

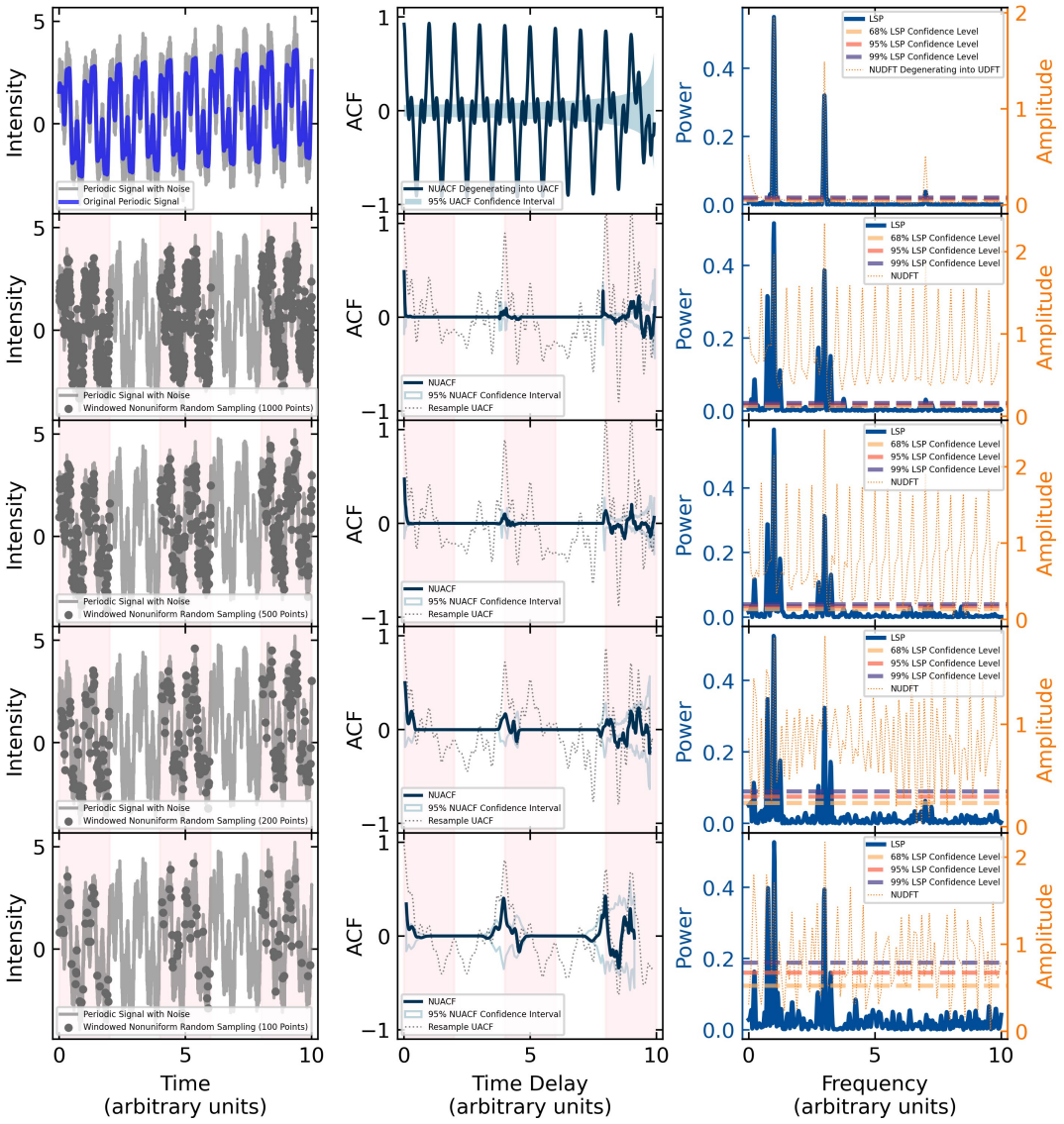


Figure 6. Comparison of resampled ACF and our NUACF: signal with a linear baseline trend. Shown here is a periodic signal (Pattern A) with an additive linear evolution trend. Our NUACF successfully identifies a portion of the repeated variability (i.e. those NUACF peaks/troughs beyond the NUACF's confidence interval), while the resampled ACF profile is biased. [The complete figure set (12 images) is available in the online journal.]

We further simulated more realistic "windowed" observations, characteristic of astronomical data sets which are interspersed with gaps due to observing constraints. For a periodic signal, we tested the impact of various windowing conditions: constant versus variable number of data points per window (Figures 5.7–5.9), different number of windows (Figures 5.10–5.12), irregular window spacing (Figures 5.13–5.15), and variable window duration (Figures 5.16–5.18). The existence of windows degrades the performance of all three methods to some extent. For the resampled and interpolated ACF, this manifests as irregular distortion in the amplitude of peaks/troughs, although their temporal spacing remains roughly periodic; this distortion becomes severe with sparse sampling. When data are sparse, they both produce severely distorted profiles, making it difficult to quantify the presence of a repetitive pattern and the associated time delay. For our NUACF, some intrinsic peaks/troughs may lose significance. From a robustness standpoint, the NUACF framework holds a distinct advantage thanks to its significance assessment by engaging the confidence interval.

Based on these initial simulations, the resampled and first-order interpolated ACF also seem to give a good performance. Given the smaller distortion of the resampled ACF under low-count conditions, we performed additional simulations to compare it directly with our NUACF. We tested scenarios including a baseline trend (Figures 6.1–6.3), high noise levels (Figures 6.4–6.6), quasi-periodic signals (Figures 6.7–6.9), and pure noise (i.e., aperiodic signal) (Figures 6.10–6.12). The NUACF's performance, while degraded, remained robust in detecting a subset of significant features, confirming its applicability even in these complex cases. In contrast, the resampled ACF applied to pure noise, particularly under sparse sampling, can produce spurious periodic-like profiles. This ambiguity makes it challenging to distinguish between a signal with a genuine repetitive variability pattern and aperiodic signal when sampling is limited.

We next evaluated the NUACF's performance on real stellar light curves from the dataset of An Expandable Light Curve Dataset for Automatic Classification of Variable Stars (LEAVES) (Fei et al. 2024). This dataset, hosted by China's National Astronomical Data Center, provides a homogeneous collection of stellar light curves by integrating data from several major surveys: the All-Sky Automated Survey for Supernovae (ASAS-SN) Catalog of Variable Stars X (Christy et al. 2023), Gaia Data Release 3 (Gaia Collaboration et al. 2023), and the Zwicky Transient Facility (ZTF) Data Release 2 (Masci et al. 2019). Despite the elaborately designed plan of these surveys, their light curves invariably exhibit significant nonuniform sampling due to observational constraints, intrinsic survey modes, and quality control. This makes them an ideal testbed for our method.

We first analyzed a Cepheid variable, CEP J052707.40-651812.6, a strictly periodic star crucial to the cosmic distance ladder (Freedman et al. 2001; Riess et al. 2022). Figure 7(a) shows its light curve over four years, with the inset highlighting the ∼10-day period, also evident in its power spectrum [Figure 7(d)]. Figure 7(b) compares the results from NUACF, resampled ACF, and first-order interpolated ACF. The NUACF, based on its 99% confidence interval, robustly identifies the repetitive pattern, with significant peaks denoted by the solid purple lines and troughs by the dashed blue lines, respectively. The other methods also reveal the pattern in their profile morphology but lack built-in significance assessment and error estimation for the time delays. Figure 7(c) shows the histogram of significant features from the MC simulations used for error estimation; features with high counts correspond to the significant peaks/troughs in panel (b).

A key methodological difference is that the resampled and interpolated ACF rely on periodically spaced features in their profile to infer a repeating pattern, whereas our NUACF identifies significant features solely based on the confidence interval (i.e., NUACF peaks exceeding the upper bound or valleys falling below the lower bound are deemed significant). This allows the NUACF to detect non-periodic repetitive patterns with irregular spacing, for which other methods without a clear confidence estimation would completely fail. The Lomb-Scargle periodogram is suitable for simple periodicity analysis (Lomb 1976; Scargle 1982; VanderPlas 2018), while our NUACF is a time-domain tool that

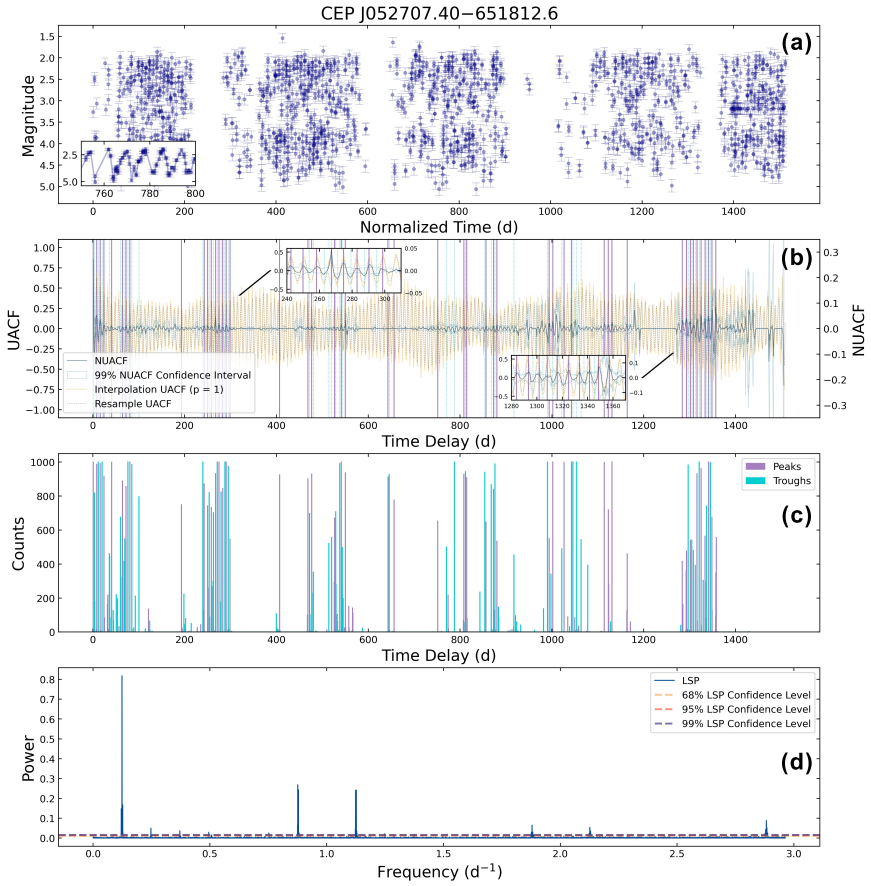


Figure 7. Application of our NUACF to a strictly periodic Cepheid variable, CEP J052707.40−651812.6. (a) Four-year light curve taken from the LEAVES dataset, with the inset zooming in on the ∼10-day period. (b) Comparison of the different autocorrelation function (ACF) methods: NUACF (dark blue line, with the 99% confidence interval shown as a blue region), resampled ACF (gray dotted line), and first-order interpolated ACF (orange line). The resampled and interpolated ACFs (collectively labeled UACF) are shown through the left vertical axis, while the NUACF refers to the right axis. The NUACF identifies significant peaks (solid purple vertical lines) and troughs (dotted blue vertical lines) outside its confidence band. The traditional methods show a periodic profile but lack a statistical criterion for significance. (c) Histogram of significant features identified across MC simulations, validating the features in panel (b) (high-count bins correspond to significant peaks/troughs). Based on this histogram and Equation (5), our NUACF are able to provide a complete error estimate for the significant time delays, while other methods cannot. (d) Corresponding Lomb-Scargle periodogram (LSP), confirming the dominant period of the light curve shown in panel (a).

can be efficiently applied to identify repetitive variability and the corresponding time delays, as illustrated in the above periodic Cepheid case.

We then analyzed a Delta Scuti variable (DSCT J061806.84-754759.0), which exhibits multi-periodic pulsations. Its light curve [Figure 8(a)] and power spectrum [Figure 8(d)] reveal eight frequency components. As shown in Figure 8(b), for such complex signals, the resampled and interpolated ACF become ineffective, while our NUACF successfully identifies multiple significant peaks and troughs via the confidence interval method. The inset of Figure 8(a) compares two light-curve segments separated by the delay of peak P1, suggesting a repeated pattern. The corresponding MC histogram is shown in Figure 8(c).

Finally, we applied the NUACF to an interesting star, AP2082775, which exhibits small-amplitude, non-periodic fluctuations [Figure 9(a) & (d)]. Remarkably, our NUACF still identifies a few significant peaks and troughs [Figure

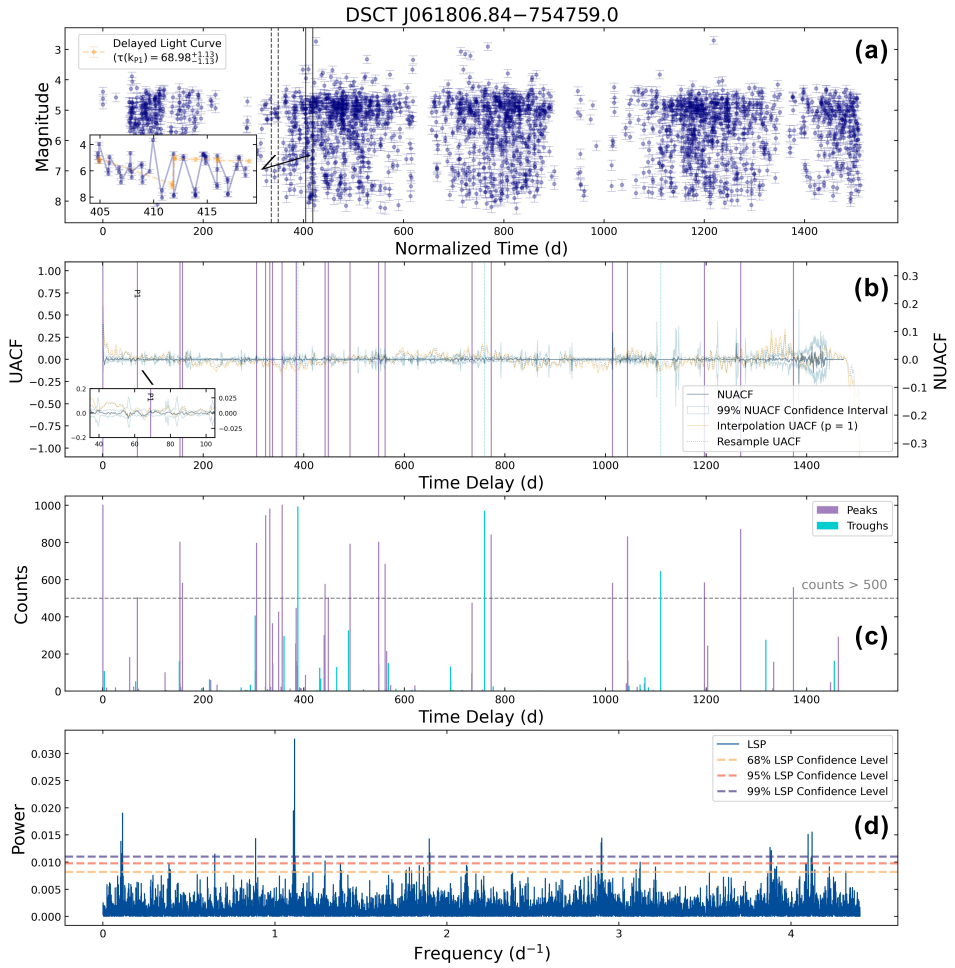


Figure 8. NUACF analysis of a multi-periodic Delta Scuti variable, DSCT J061806.84-754759.0. (a) Light curve of the star. The inset compares two segments separated by the time delay of the significant NUACF peak P1, suggesting a repeated pattern. (b) Results of different ACF methods. The resampled (gray dotted line) and interpolated (orange line) ACFs fail to produce a clear interpretable pattern for this complex signal. In contrast, our NUACF (dark blue line, with the 99% confidence interval shown as the blue region) identifies multiple significant peaks (solid vertical purple lines) and troughs (dotted blue vertical lines). (c) MC histogram of significant NUACF features, corroborating the features in panel (b) that were derived from the central flux measurements. (d) LSP analysis revealing eight frequency components.

9(b)], which are validated by the MC simulations [Figure 9(c)]. The inset of Figure 9(a) compares two segments separated by the delay of peak P1, showing a possible match.

Iterative application of the ACF (i.e., applying the ACF to its own output) can act as a filter, potentially purifying the light curve's dominant frequency. Figure 10 compares this effect for different methods on a noisy, nonuniformly sampled periodic signal. As the iteration order (o) increases, the structure of NUACF profile becomes more prominent, revealing the potential dominant frequency component. However, higher orders are not always better. Figure 11 shows that even for pure noise cases, a high-order NUACF still produces a structured profile. This occurs because the iterative process acts as a low-pass filter, progressively attenuating high-frequency components in the light curve, regardless of whether they are periodic or not. Given enough iterations, this process inevitably yields a regular shape. We therefore recommend limiting NUACF iteration to order 2 in practice. Figures 12–15 test the impact of windowed observations on iterated NUACF for periodic, quasi-periodic, severely noisy quasi-periodic, and aperiodic signals. The second-order NUACF performs well across these cases. In the frequency domain (panels (b) of these figures), the second-order

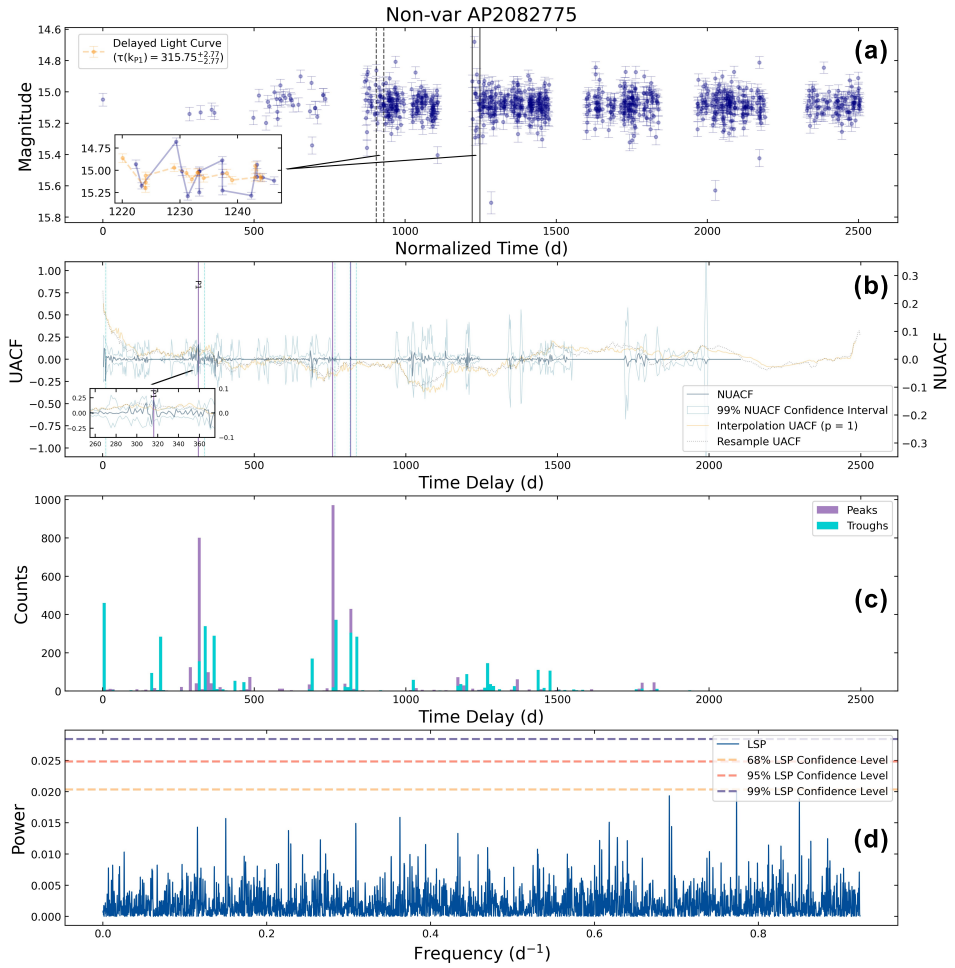


Figure 9. NUACF applied to a non-variable star, AP2082775. (a) Light curve exhibiting small-amplitude, non-periodic fluctuations. The inset compares two segments separated by the delay of the most significant NUACF peak, P1, showing a possible repetition in the activity. (b) The NUACF (dark blue line, with the 99% confidence interval shown as the blue region) identifies a number of significant peaks (e.g., P1) and troughs, whereas the resampled and interpolated ACFs show no clear pattern. (c) MC histogram confirming that the detected NUACF features are statistically robust. (d) The corresponding LSP shows no periodicity.

NUACF power spectrum purifies the dominant frequency compared to the first order. However, from the third order onward, the spectrum distorts, exhibiting amplified low-frequency components and axis-symmetric artifacts.

Now we turn to the application of NUCCF. Let us consider the application of CCF in AGN reverberation mapping. In this framework, the time delay between the UV/optical continuum light curve (connected to the accretion disk) and the broad emission-line light curve (relevant to the surrounding gas in the broad-line region) is measured, providing constraints on the black hole mass and the size of the broad-line region. We first performed a test through simulations. Figure 16(a) shows the simulated seed (Band 1) and response (Band 2) light curves with an intrinsic delay of 3.55 days. Figure 16(b) shows that the NUCCF, DCF, interpolated CCF, and resampled CCF all peak near the pre-assumed delay, but only our NUCCF provides an error estimate, as it quantifies the uncertainty arising from sampling irregularity itself. Reducing the sampling of the response band (Figure 17) or both bands equally (Figure 18) reveals two distinct effects: a large disparity in sampling counts between the two light curves primarily degrades the NUCCF's

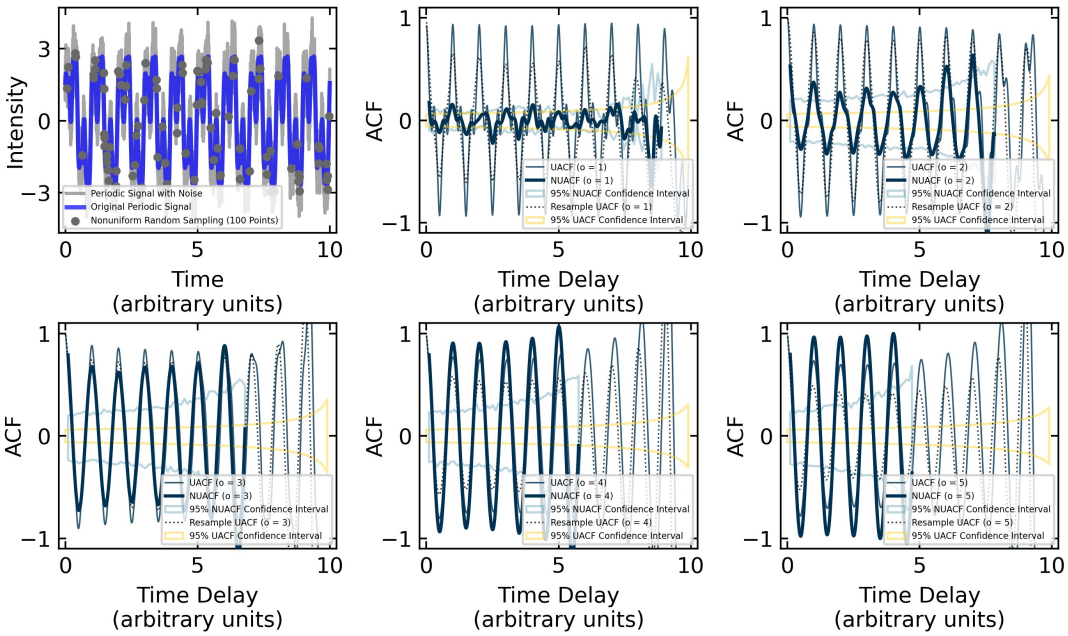


Figure 10. Iterated NUACF as a filter on a noisy, nonuniformly sampled periodic signal. The iterative filtering effects for different ACF methods are compared. The top-left panel shows the input: a simulated periodic signal (Pattern A) with added noise, sampled nonuniformly. The resampled ACF and our NUACF are applied to this nonuniform data; the standard sample ACF is applied to a densely and uniformly sampled, quasi-continuous version of the same underlying signal. Profiles are shown for iteration orders $o = 1$ to 5 for the three methods, i.e. our NUACF (thick dark blue line, with a 95% confidence interval shown as light blue region), resampled ACF (black dotted line), and standard sample ACF (thin dark blue line, with a 95% confidence band shown as yellow region). Here, $o = 1$ is the result of applying the ACF method directly to the data; $o = 2$ is obtained by applying the same method to the $o = 1$ result, and so forth. As the iteration order o increases, the NUACF profile becomes smoother and more regular, suggesting a purification of the light curve's dominant frequency.

significance (the extent to which the peak exceeds the confidence interval), while a lower total sampling count is the dominant factor increasing the uncertainty in the time delay.

To demonstrate NUCCF's utility for modern reverberation mapping, which increasingly employs dense, multi-band monitoring to probe smaller length scales of the central engine (Pal et al. 2017; Hernández Santisteban et al. 2020a), we apply the NUCCF to the intensive, multi-wavelength light curves of the AGN Fairall 9 [Figure 19(a); Hernández Santisteban et al. 2020a]. Figure 19(b) compares the measured time delays of other bands relative to the W2 band obtained with different methods, including the DCF and our NUCCF, as well as the interpolated CCF and the CREAM model-fitting method as employed in the original authors' study (Starkey et al. 2016, 2017). The DCF fails to provide meaningful constraints, as it gives nearly zero delay for all the bands. Our NUCCF agrees with the other two methods in 7 out of 13 bands. In some bands, notably W1, it suggests a delay of opposite sign with high significance. While our NUCCF is intrinsically data-faithful, this case further highlights that conclusions drawn from finite data can be contentious.

We also explore the application of NUCCF in gravitational lensing, in which the time delay between multiple images of a lensed quasar (created when its light is bent by a foreground massive galaxy) provides geometric constraints on cosmological parameters (Tewes et al. 2013; Bonvin et al. 2017; Wong et al. 2020). Let us take the renowned quadruply lensed quasar HE 0435−1223 (Bonvin et al. 2017) as an example, which is a system with over a decade of monitoring. The results are shown in Figure 20, while Figure 21 presents a comparison of the performance for different CCF methods. In this long-baseline but sparsely sampled case (with a mean sampling interval of ∼5 days), our NUCCF

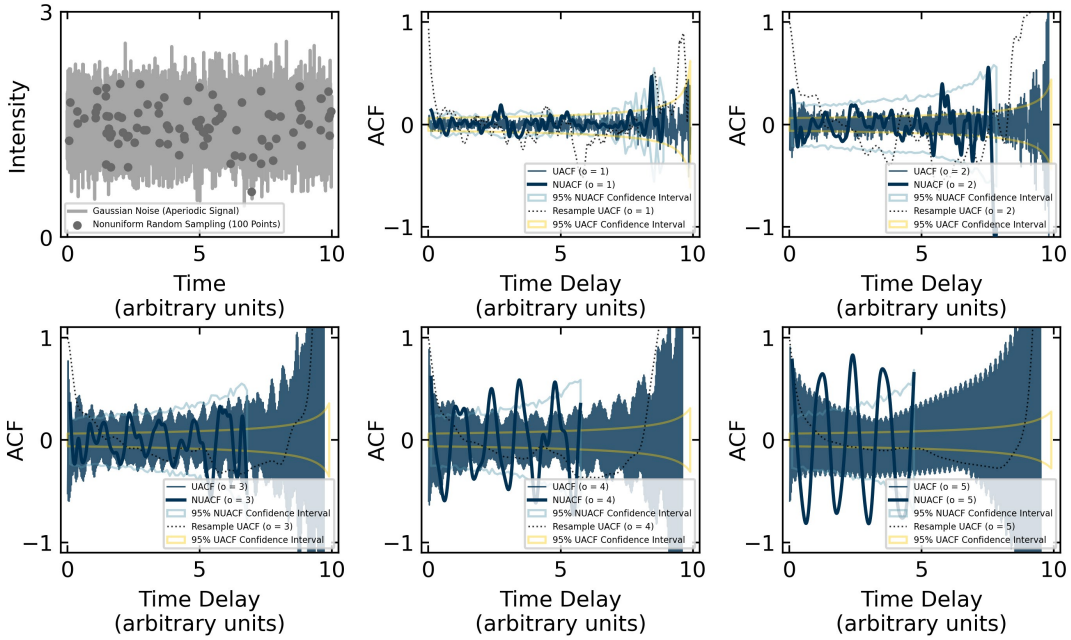


Figure 11. Spurious regularity from high-order NUACF applied to pure noise (aperiodic signal). Shown here is iterative NUACF applied to a time series of pure Gaussian noise, which can be treated as a kind of aperiodic signal. While the first-order NUACF ($o = 1$) correctly shows no significant structure, higher iterations ($o \geq 3$) produce progressively smoother, regular profiles. This confirms that beyond its intended role in isolating the dominant frequency, iterative NUACF acts as a strong low-pass filter. In practice, we therefore recommend limiting iteration to order $o = 2$. At higher orders, the iterative process indiscriminately suppresses high-frequency components and amplifies low-frequency power. Under high iterations, this will inevitably produce a regular profile even from pure noise.

yields correlation peaks that are broad in width and centered near zero delay. We therefore use the width of these significant peaks to define a reliable, significance-tested range for the true time delay. This highlights a key, context-dependent trade-off: while specialized, model-fitting techniques like free-knot splines and regression differences (Tewes et al. 2013), tailored specifically to the intrinsic variability of lensed quasars, can leverage the rich dataset to provide more precise time-delay estimates with smaller formal errors, the NUCCF provides a robust, model-agnostic bound. For HE 0435−1223, our simulations define a delay range from the NUCCF that is significant at $> 4\sigma$. The time-delay estimates from the two dedicated model-fitting methods both lie within this range, providing an independent, data-driven validation of their results at this confidence level. This illustrates that even in cases where the precision is limited by sparse sampling, our NUCCF still offers a complementary, model-independent constraint for validating results from more specialized techniques.

5. SUMMARY

In summary, our NUACF/NUCCF method can effectively solve the problem induced by nonuniform sampling in astronomical observations. It performs the correlation analysis directly by treating the nonuniform sampling as a kind of temporal noise, incorporating it directly into the confidence-band construction (which thus naturally renders the band irregular). We then use such a band to assess whether the repeating variability patterns exist. In this way, we do not need to eliminate the sampling irregularity via resampling or interpolation. Our analytic formulation integrates robust significance assessment and complete error estimation, both of which are generally lacking in traditional approaches. This enables the method to function effectively across diverse astrophysical contexts, serving as a model-agnostic tool and providing a robust, scalable foundation for analyzing large and complex datasets.

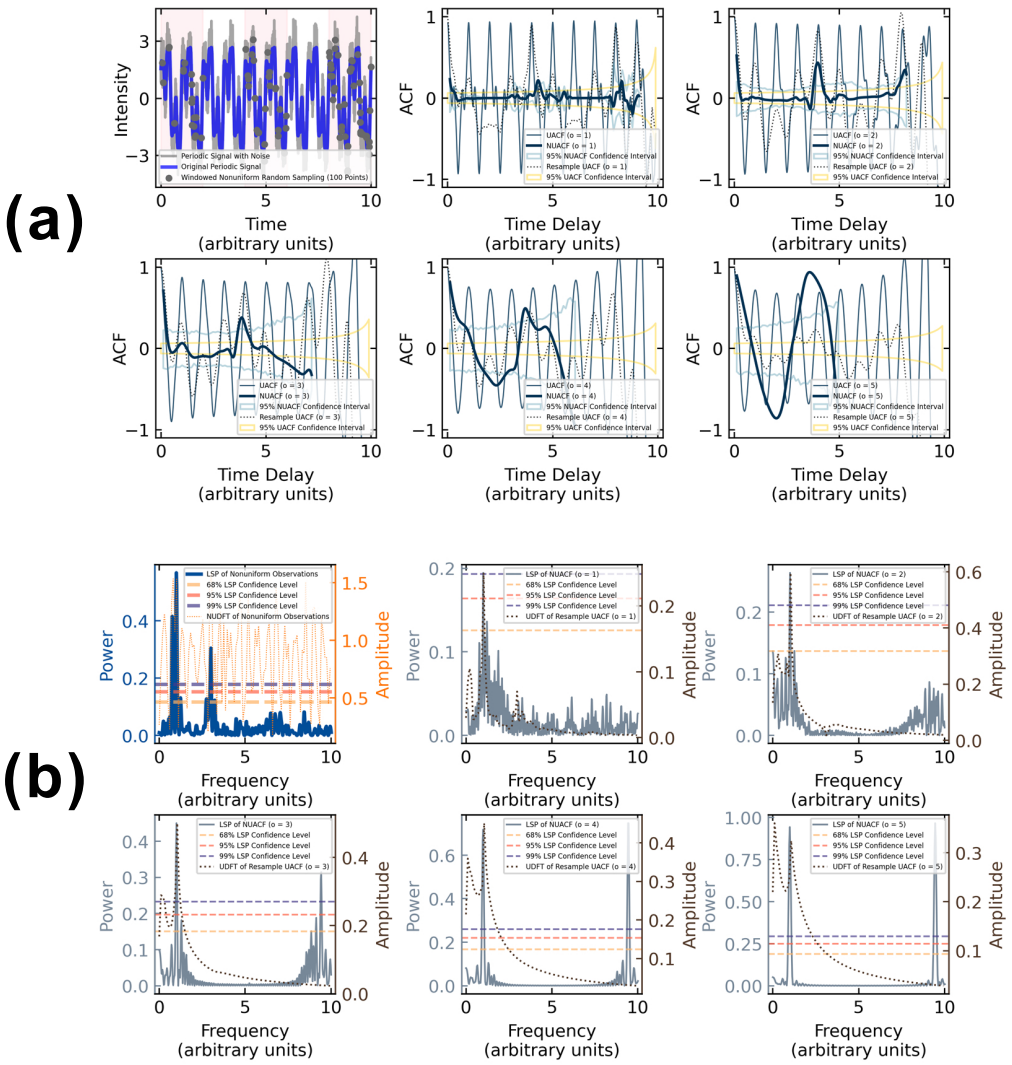


Figure 12. Impact of windowed observations on iterated NUACF: periodic signal. (a) Time-domain profiles of different ACF methods for iteration orders $o = 1$ to 5 applied to a windowed version of a periodic signal (Pattern A). The second-order NUACF ($o = 2$) effectively purifies the dominant frequency; higher orders distort the profile and shift the peak locations. (b) Corresponding power spectra of panel (a), derived from LSP (left axis) and NUDFT (right axis). The second-order NUACF spectrum sharpens the dominant peak, but from the third order onward, the spectrum distorts with amplified low-frequency power and symmetric artifacts.

It is worth noting that our method also has its own limitations. As demonstrated in our simulation tests, strongly windowed observations and sparse sampling can degrade NUACF performance. For the NUCCF, a large disparity in sampling counts between the two light curves primarily reduces the significance of the detected peak, while a low total sampling count increases the uncertainty of the measured time delay. In practice, these limitations could be mitigated by improving the quality of the observational data.

In the context of gravitational lens time-delay measurements, for instance, dedicated model-fitting methods can often provide more precise time-delay estimates with smaller formal errors, whereas our method offers a model-independent, analytically grounded cross-check that can assess the significance of such results and help validate them.

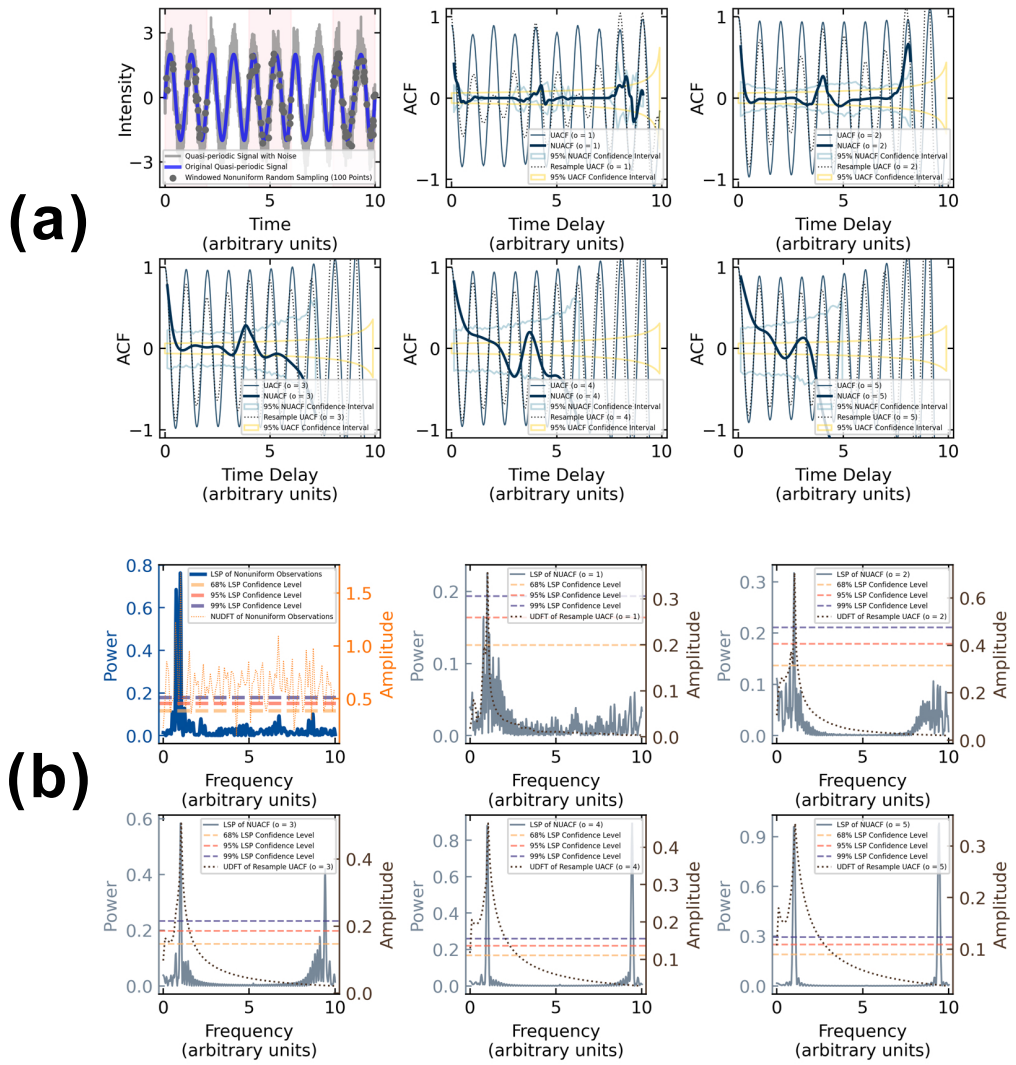


Figure 13. Impact of windowed observations on iterated NUACF: quasi-periodic signal. This figure is similar to Figure 12, but for a modulated (quasi-periodic) signal. The second-order NUACF successfully enhances the dominant pattern. Higher orders degrade the time-domain profile and introduce strong spectral distortions.

As a natural extension, our framework can also be readily extended to investigate other nascent time-domain astrophysical sources, including FRBs, by probing the relationship between persistent radio source luminosity and the activity of repeating FRBs (Li et al. 2026), or examining the interconnections among the various physical variability curves intrinsic to FRB radiation.

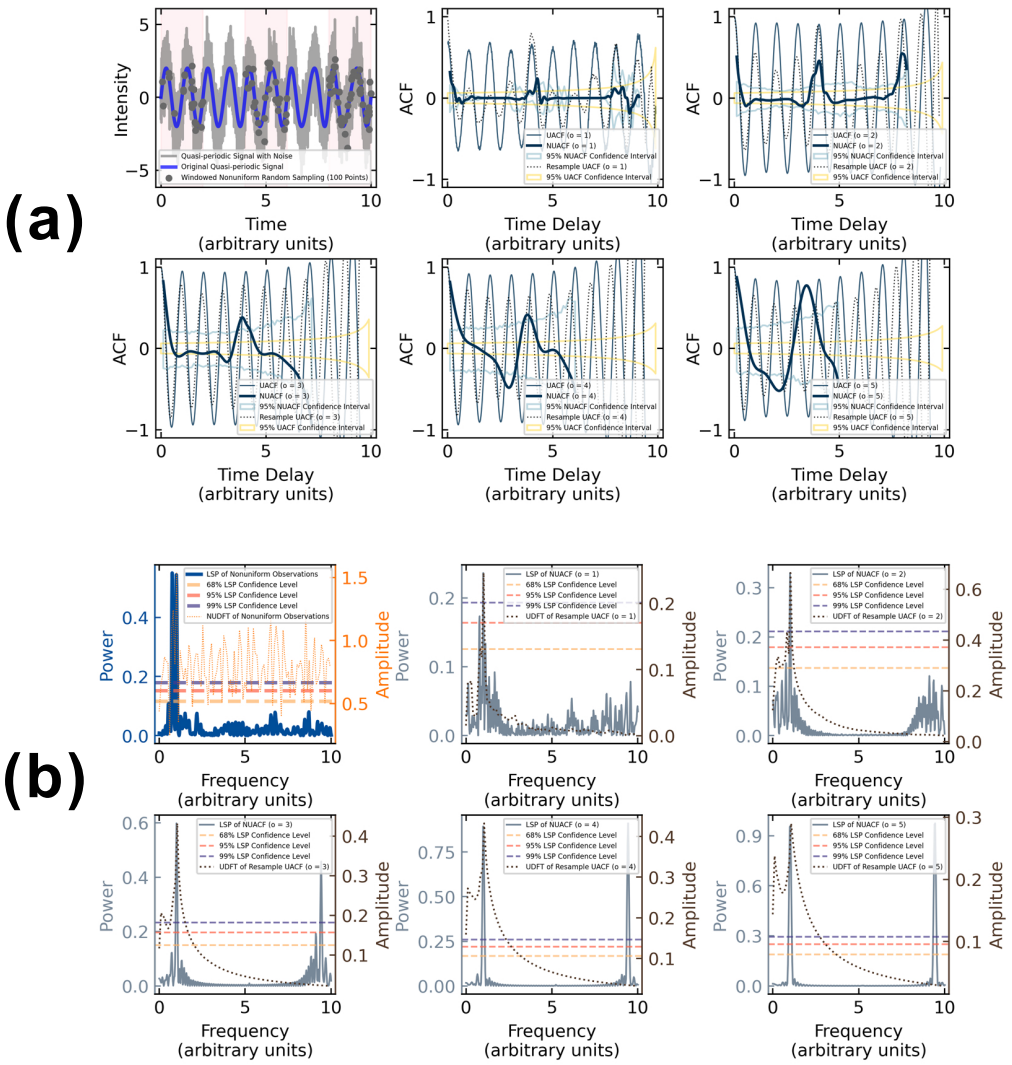


Figure 14. Impact of windowed observations on iterated NUACF: severely noisy quasi-periodic signal. Performance on a quasi-periodic signal (the same signal as in Figure 13) with high noise contamination is shown. The second-order NUACF remains the most reliable, extracting a cleaner pattern than the first order. Higher iterations amplify noise artifacts and produce misleadingly smooth profiles in both time and frequency domains.

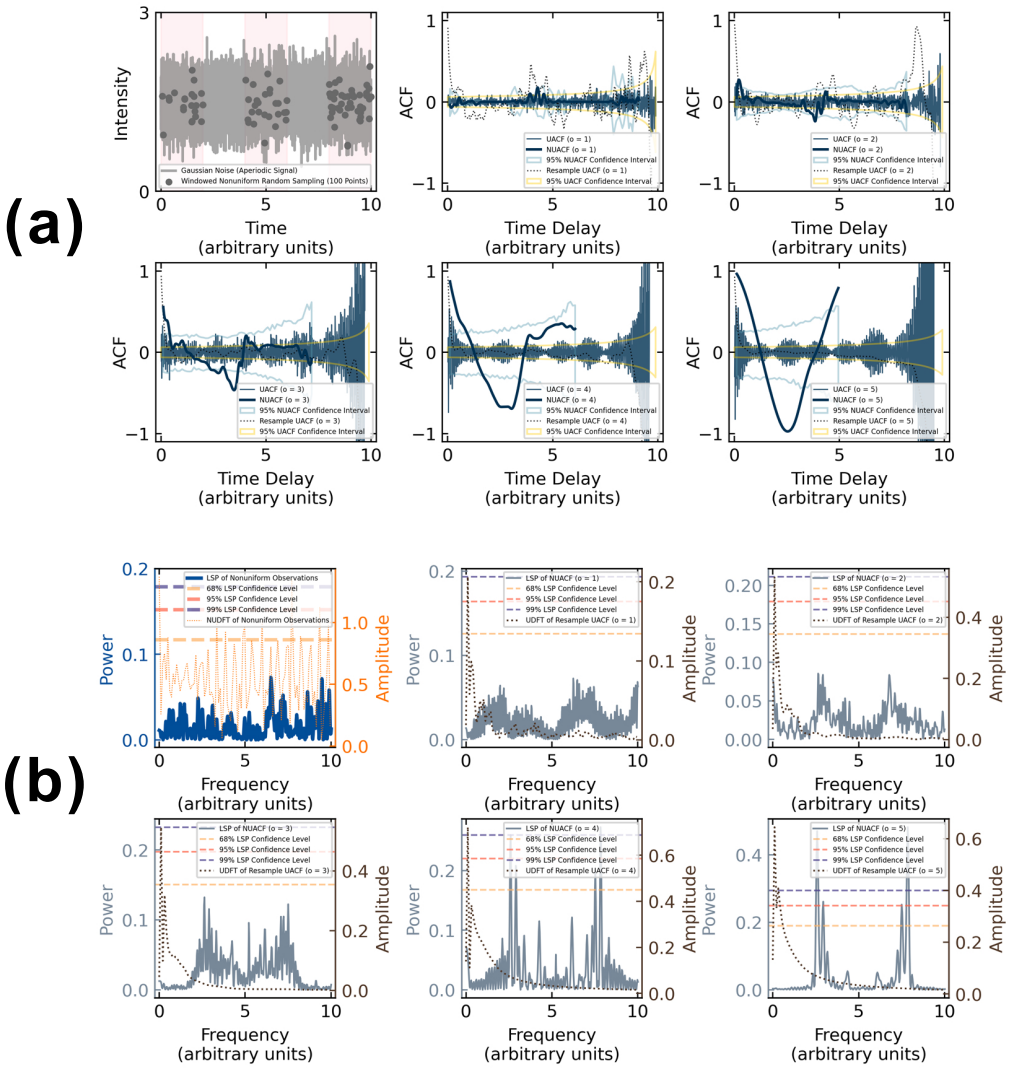


Figure 15. Impact of windowed observations on iterated NUACF: pure noise case (aperiodic signal). Application to pure noise under windowed sampling is shown. The first- and second-order NUACF correctly show no significant correlated structure. For orders $o \geq 3$, the iterative filtering creates a smooth, apparently regular profile and an asymmetric power spectrum, confirming that high-order iterations generically produce artifacts.

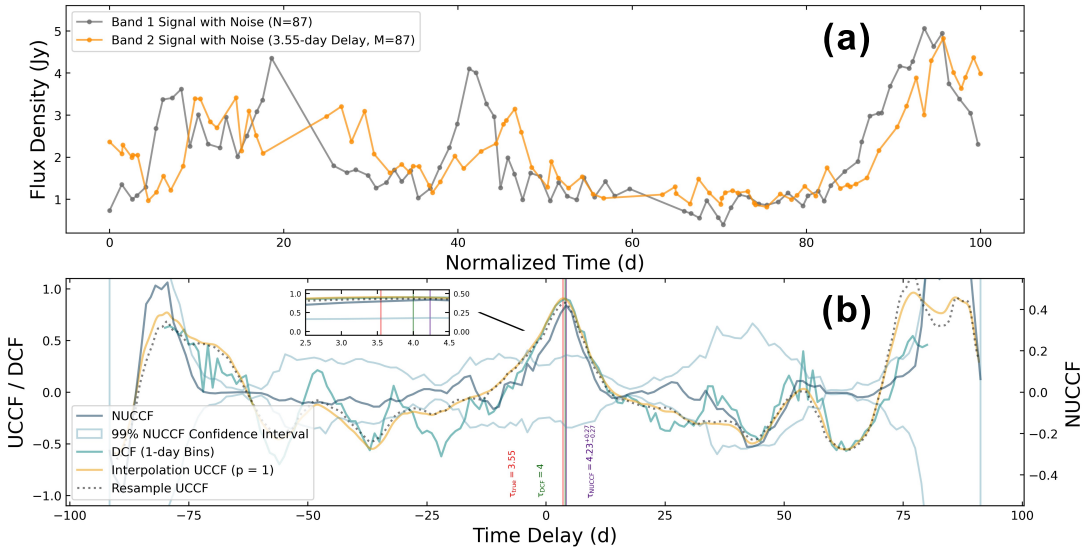


Figure 16. Simulation of reverberation mapping with a pre-assumed time delay. (a) Simulated, nonuniformly sampled light curves of the seed continuum (Band 1, gray) and the response emission line (Band 2, orange) with an intrinsic delay of 3.55 days, each with 87 sampling points. (b) CCF analysis obtained through four different methods: our NUCCF (dark blue line with 99% confidence interval shown as blue region), DCF (green line), first-order interpolated CCF (yellow line), and resampled CCF (gray dotted line). All methods peak near the pre-assumed delay time, but only the NUCCF provides an error estimate that directly quantifies the uncertainty arising from sampling irregularity.

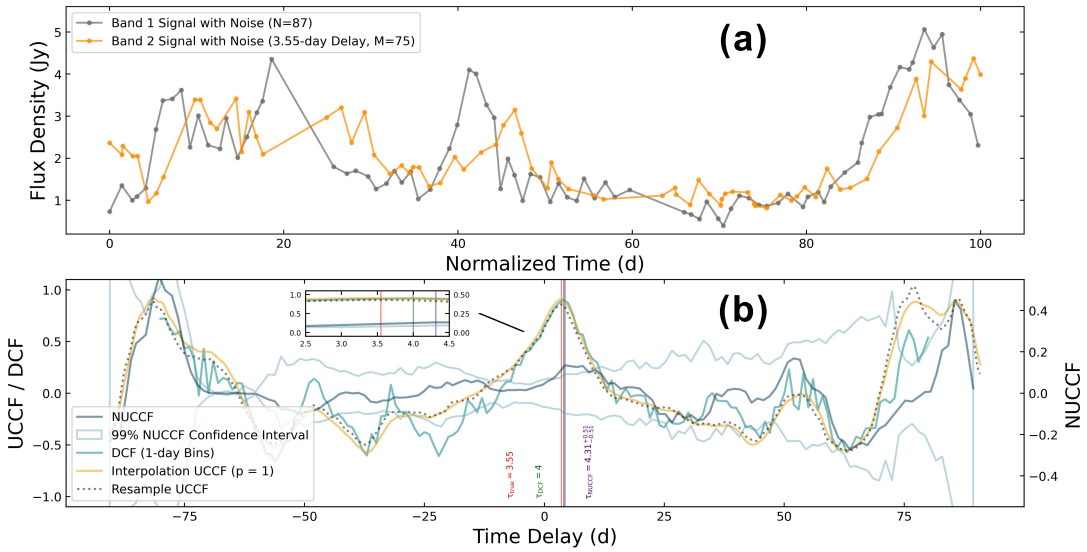


Figure 17. Effects of reducing the sampling frequency of the response band only. This figure is similar to Figure 16, but the response band (Band 2) is more sparsely sampled than the seed band (Band 1). The disparity in sampling counts between the two bands primarily degrades the significance of the NUCCF peak (i.e., the height of the peak relative to its confidence interval), while the peak position remains close to the intrinsic delay.

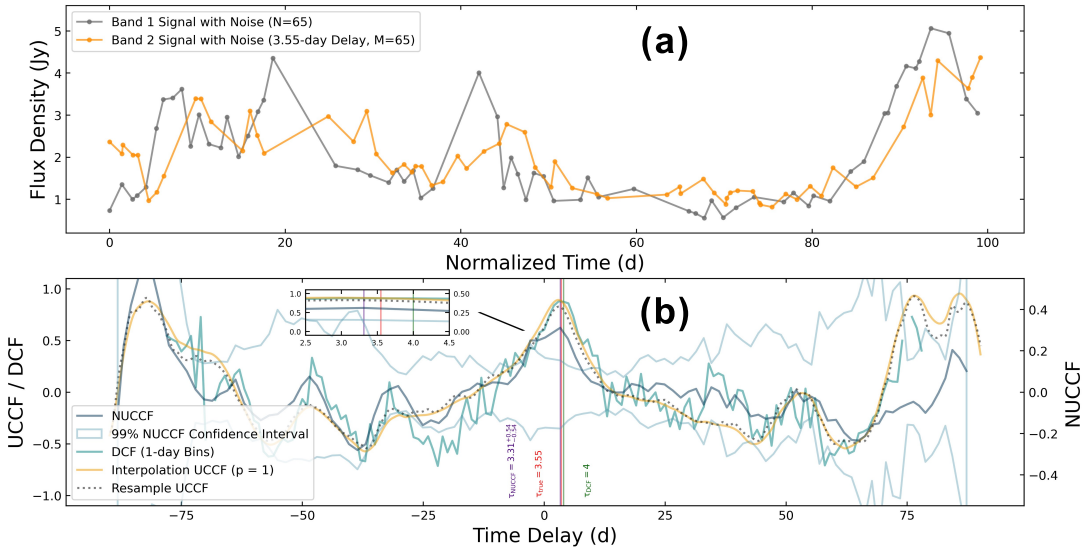


Figure 18. Effects of reducing the sampling frequency of both bands equally. This figure is similar to Figure 16, but with equally reduced sampling in both the seed (Band 1) and response (Band 2) bands. The smaller total sampling count increases the uncertainty in the time delay estimate [see Equation (9)]. However, because the sampling counts of the two bands remain equal here, the significance of the NUCCF peak is higher than that in Figure 17 (where the two bands have unequal sampling counts), though still lower than that in Figure 16 (which has the highest total sampling counts).

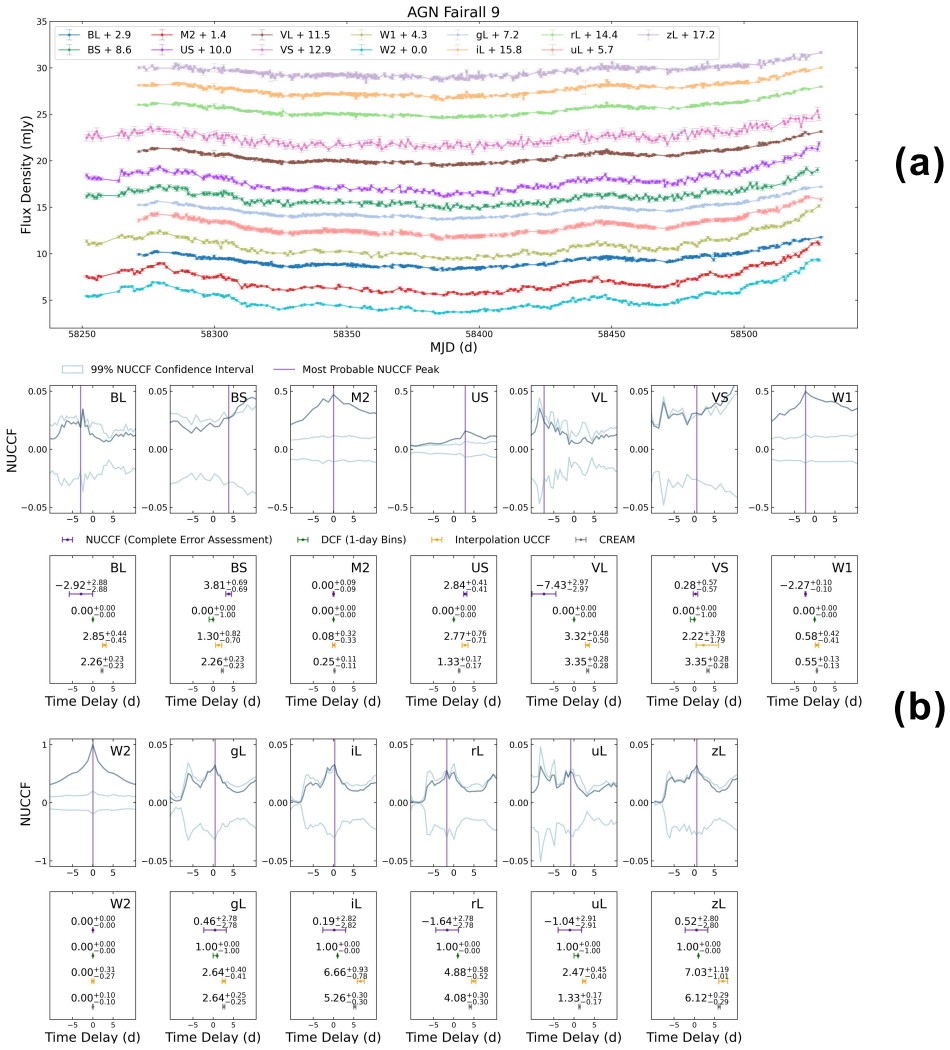


Figure 19. Application of our NUCCF to a special AGN, Fairall 9. (a) Intensive, multi-wavelength continuum light curves of Fairall 9 from a disc-reverberation mapping campaign (Hernández Santisteban et al. 2020a). (b) Comparison of time delays of 13 bands relative to the W2 band, derived by using four different methods. First/third rows: NUCCF (dark blue line) with 99% confidence interval (blue region) and the highest MC-derived peak (purple line). Second/fourth rows: NUCCF delay (purple) vs. DCF (green), interpolated CCF (yellow, original-study method), and CREAM model-fitting (gray, original-study method). The DCF yields nearly zero delays for all bands, failing to provide meaningful constraints. The NUCCF agrees with the interpolated CCF and CREAM results in 7 of the 13 bands. In several bands (most significantly in W1), our NUCCF indicates a delay of the opposite sign.

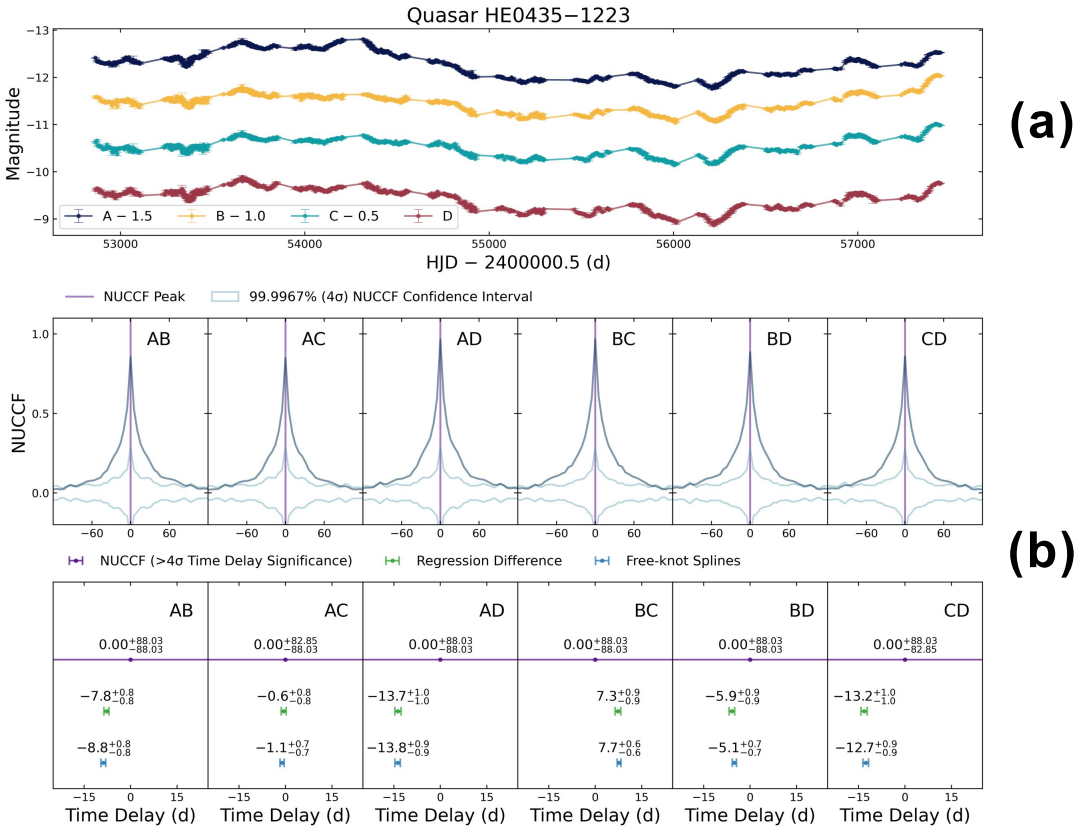


Figure 20. Our NUCCF analysis of the lensed quasar HE 0435−1223. (a) Light curves of the four lensed images (A, B, C, D) of the quasar, spanning over a decade of monitoring with a mean sampling interval of ∼5 days (data from Bonvin et al. (2017)). (b) Results of different methods for the time delays between image pairs. Following the original study, the light curves were preprocessed with `PyCS3` to mitigate microlensing effects. First row: Our NUCCF result (dark blue line) with 4σ confidence interval (blue region) and MC-derived most probable peak (purple line). Second row: our NUCCF delay (purple) vs. regression difference model-fitting (green, original-study method), and free-knot splines model-fitting (blue, original-study method). In this long-baseline, sparsely sampled regime, our NUCCF produces broad peaks centered near zero delay. The width of these significant peaks defines a reliable, significance-tested range (indicated by purple horizontal bars) for the true time delay, providing an independent model-agnostic constraint.

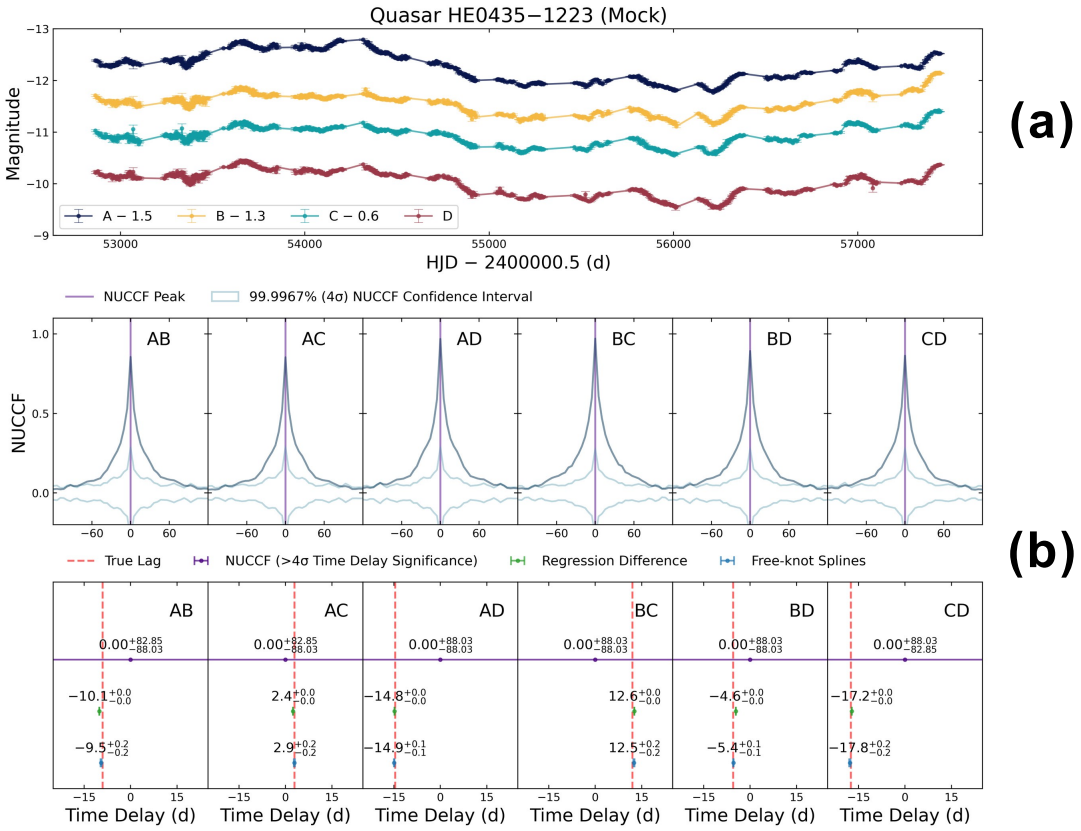


Figure 21. Comparing our NUCCF method with other dedicated model-fitting methods using simulated light curves based on observational data of HE 0435−1223. This figure is similar to Figure 20, but using simulated light curves replicating the sampling and variability characteristics of HE 0435-1223 [simulated data are taken from Bonvin et al. (2017)]. The two specialized, model-fitting techniques (free-knot splines and regression differences), employed in the original study, provides precise estimates for the time delays. Both model-fitting estimates fall within our NUCCF-defined range, offering an independent, data-driven validation (i.e. $>4\sigma$ significance) of their results. This illustrates the effectiveness of our NUCCF as a model-independent tool.

DATA AVAILABILITY

All simulations evaluating the performance of the NUACF and NUCCF were conducted using synthetic data generated by code, without employing observational data. The stellar light curves used to validate the NUACF performance were sourced from the LEAVES dataset (Yu 2024; available at https://nadc.china-vo.org/res/r100962/; also see the survey paper of Fei et al. 2024). Hosted by China's National Astronomical Data Center, the LEAVES dataset integrates stellar light curves from several major surveys: ASAS-SN Catalog of Variable Stars X (Christy et al. 2023; https://asas-sn.osu.edu/variables), Gaia Data Release 3 (Gaia Collaboration et al. 2023; https://www.cosmos.esa.int/web/gaia/dr3), and ZTF Data Release 2 (Masci et al. 2019; https://irsa.ipac.caltech.edu/Missions/ztf.html). The AGN Fairall 9 data used to validate the performance of NUCCF were obtained from Hernández Santisteban et al. (2020a) (also see Hernández Santisteban et al. 2020b; the multi-band light curves are available at https://zenodo.org/records/3956577), while the light curves for the four images of the lensed quasar HE 0435−1223 were sourced from Bonvin et al. (2017) and are publicly available at https://shsuyu.github.io/H0LiCOW/site/h0licow_data.html.

CODE AVAILABILITY

Results can be fully reproduced using the methodology described in Methods. All analysis scripts and source code, along with all observational data used in this study, have been deposited in Zenodo (https://doi.org/10.5281/zenodo.20809667) for reproducibility. The package also includes standalone implementations of the NUACF and NUCCF tools.

Furthermore, the PyCS3 software toolbox used to preprocess the light curves of the lensed quasar images by mitigating microlensing effects is available at https://gitlab.com/cosmograil/PyCS3/. PyCS3 also provides the two specialized model-fitting approaches (regression difference and free-knot splines) used in the original study to extract time delays.

ACKNOWLEDGMENTS

We are grateful to the anonymous referee for valuable comments and suggestions. This study is supported by the National Natural Science Foundation of China (Grant Nos. 12233002, 12622309, 12273113) and by the National Key R&D Program of China (2021YFA0718500). Y.-F.H. also acknowledges the support from the Xinjiang Tianchi Program. J.-J.G. acknowledges support from the Youth Innovation Promotion Association (2023331). O.A. was also supported by the Project funded by China Postdoctoral Science Foundation (Grant No. 2025M783225).

APPENDIX

A. DERIVATION OF THE NONUNIFORM AUTOCORRELATION FUNCTION

Traditional normalized ACF can be conveniently calculated for uniformly sampled discrete timing sequences. Correspondingly, our NUACF is a further extension of ACF from the uniform discrete domain to the nonuniform discrete domain, bridging the gap between idealized and real observational conditions.

To clarify the logic of this extension, we begin with a familiar concept, variance, and examine its formulation in both continuous and discrete domains. For a continuous time series $x(t)$, the variance is defined as

$$\sigma_{\mathrm{C}}^2 = \lim_{T\to\infty} \frac{1}{2T} \int_{-T}^{T} \left[x(t) - \overline{x(t)}\right]^2 \mathrm{d}t, \tag{A1}$$

where $\overline{x(t)}$ denotes the mean of $x(t)$. For a finite observation duration, Equation (A1) becomes

$$\sigma_{\mathrm{C}}^2 = \frac{1}{T} \int_{0}^{T} \left[x(t) - \overline{x(t)}\right]^2 \mathrm{d}t. \tag{A2}$$

Discretizing Equation (A2) yields

$$\sigma_{\mathrm{D}}^2 = \frac{1}{t_N - t_1} \sum_{i=1}^{N} (x_i - \bar{x})^2 \Delta t_i, \tag{A3}$$

where Δt_i represents the time interval of the i-th observation, and N is the total number of observations.

For uniformly sampled data where $\Delta t_i = \Delta t$ is constant, we have $t_N - t_1 = (N-1)\Delta t$, and Equation (A3) reduces to the common unbiased sample variance:

$$\sigma_{\mathrm{D,U}}^2 = \frac{1}{N-1} \sum_{i=1}^{N} (x_i - \bar{x})^2 . \tag{A4}$$

For nonuniformly sampled data, we apply the trapezoidal rule to Equation (A3), obtaining the nonuniform variance estimator:

$$\sigma_{\mathrm{D,NU}}^2 = \frac{1}{t_N - t_1} \left[\sum_{i=2}^{N-1} (x_i - \bar{x})^2 \frac{t_{i+1} - t_{i-1}}{2} + (x_1 - \bar{x})^2 \frac{t_2 - t_1}{2} + (x_N - \bar{x})^2 \frac{t_N - t_{N-1}}{2} \right]. \tag{A5}$$

The variance refers to the spread of a continuous variable in the time domain (i.e., the L^2 norm of a continuous function), rather than the one in static statistics (e.g., the spread of student heights in a classroom). This example illustrates how the transition from the continuous to the discrete domain differs between uniform and nonuniform sampling. In the continuous domain, time matters; under uniform sampling, the time-related terms cancel, yielding the explicitly time-independent mathematical expression; under nonuniform sampling, they do not cancel, and the time dependence explicitly remains.

We now consider the ACF. For a stationary discrete series (i.e., one whose statistical moments, such as the mean and variance, are time-invariant), the standard unbiased sample ACF under uniform sampling is

$$\mathrm{acf}_{\mathrm{D,U}}(k) = \frac{N}{N-k} \frac{\sum_{i=1}^{N-k} (x_i - \bar{x})(x_{i+k} - \bar{x})}{\sum_{i=1}^{N} (x_i - \bar{x})^2}, \quad k \in \mathbb{N}, k \le N - 10, \tag{A6}$$

where k is the lag in observation number. For uniform sampling, shifting the series by k points aligns the delayed series perfectly with the original series, resulting in $N-k$ matched pairs. The corresponding time delay is $\tau_{\mathrm{D,U}}(k) = k\frac{t_n - t_1}{N-1}$.

For nonuniform sampling, however, a simple shift by k positions (i.e., k data points) in the sequence does not produce temporally aligned pairs (see Figure 2). This presents two challenges: (i) determining an optimal trial time delay $\tau_{\mathrm{D,NU}}(k)$ that minimizes the overall temporal misalignment between the delayed and original series for a given trial index lag k, and (ii) robustly comparing the resulting misaligned pairs.

Assuming for the moment that the optimal trial time delay $\tau_{\mathrm{D,NU}}(k)$ is known, we address the second challenge by introducing a pair-centered time axis. The representative time for the i-th pair is defined as $\{[t_i + \tau_{\mathrm{D,NU}}(k)] + t_{i+k}\}/2$ (gray dashed line in Figure 2). A weight w_i is also introduced to penalize the residual temporal offset within each pair, $|[t_i + \tau_{\mathrm{D,NU}}(k)] - t_{i+k}|$. Following the same logic that extends Equation (A4) to Equation (A5), we generalize the standard sample ACF in Equation (A6) to the nonuniform domain:

$$
\begin{aligned}
\mathrm{acf}_{\mathrm{D,NU}}(k) = {} & \left[\left\{1/\left[\frac{t_{N-k}+\tau_{\mathrm{D,NU}}(k)+t_N}{2} - \frac{t_1+\tau_{\mathrm{D,NU}}(k)+t_{k+1}}{2}\right]\right\}\right. \\
& \left(\sum_{i=2}^{N-k-1}(x_i-\bar{x})(x_{i+k}-\bar{x})\left\{\frac{1}{2}\left[\frac{t_{i+1}+\tau_{\mathrm{D,NU}}(k)+t_{i+k+1}}{2} - \frac{t_{i-1}+\tau_{\mathrm{D,NU}}(k)+t_{i+k-1}}{2}\right]\right\} w_i\right. \\
& + (x_1-\bar{x})(x_{k+1}-\bar{x})\left\{\frac{1}{2}\left[\frac{t_2+\tau_{\mathrm{D,NU}}(k)+t_{k+2}}{2} - \frac{t_1+\tau_{\mathrm{D,NU}}(k)+t_{k+1}}{2}\right]\right\} w_1 \\
& \left.\left. + (x_{N-k}-\bar{x})(x_N-\bar{x})\left\{\frac{1}{2}\left[\frac{t_{N-k}+\tau_{\mathrm{D,NU}}(k)+t_N}{2} - \frac{t_{N-k-1}+\tau_{\mathrm{D,NU}}(k)+t_{N-1}}{2}\right]\right\} w_{N-k}\right)\right] \\
& / \left([1/(t_N-t_1)]\left\{\sum_{i=2}^{N-1}(x_i-\bar{x})^2\left[\frac{1}{2}(t_{i+1}-t_{i-1})\right] + (x_1-\bar{x})^2\left[\frac{1}{2}(t_2-t_1)\right] + (x_N-\bar{x})^2\left[\frac{1}{2}(t_N-t_{N-1})\right]\right\}\right) \qquad \text{(A7)} \\
= {} & \left((t_N-t_1)\left\{\sum_{i=2}^{N-k-1}(x_i-\bar{x})(x_{i+k}-\bar{x})[(t_{i+1}-t_{i-1})+(t_{i+k+1}-t_{i+k-1})] w_i\right.\right. \\
& + (x_1-\bar{x})(x_{k+1}-\bar{x})[(t_2-t_1)+(t_{k+2}-t_{k+1})] w_1 \\
& \left.\left. + (x_{N-k}-\bar{x})(x_N-\bar{x})[(t_{N-k}-t_{N-k-1})+(t_N-t_{N-1})] w_{N-k}\right\}\right) \\
& / \left\{[(t_{N-k}-t_1)+(t_N-t_{k+1})]\left[\sum_{i=2}^{N-1}(x_i-\bar{x})^2(t_{i+1}-t_{i-1}) + (x_1-\bar{x})^2(t_2-t_1) + (x_N-\bar{x})^2(t_N-t_{N-1})\right]\right\}, \\
& k \in \mathbb{N}, k \le N-10,
\end{aligned}
$$

where the misalignment weight $w_i = \exp\left\{-\frac{(N-1)^2[t_i - t_{i+k} + \tau_{\mathrm{D,NU}}(k)]^2}{(t_N-t_1)^2}\right\}$ is chosen as a Gaussian kernel. This weight quantifies the specific temporal offset within each pair, normalized by the mean sampling interval.

Note that the pair-centered time axis we just mentioned is introduced purely as a virtual computational device to assign a representative time to each misaligned pair. Its explicit dependence is algebraically removed in the final expression of Equation (A7) [see the cancellation of $\tau_{\mathrm{D,NU}}(k)$ from the second to the sixth line of Equation (A7)].

We then determine the optimal trial time delay $\tau_{\mathrm{D,NU}}(k)$. Under uniform sampling, Equation (A7) reduces to

$$
\begin{aligned}
\mathrm{acf}_{\mathrm{D,NU}\to\mathrm{U}}(k) = {} & \left((N-1)\left[\sum_{i=2}^{N-k-1}(x_i-\bar{x})(x_{i+k}-\bar{x})\cdot 4 + (x_1-\bar{x})(x_{k+1}-\bar{x})\cdot 2 + (x_{N-k}-\bar{x})(x_N-\bar{x})\cdot 2\right]\right. \\
& \left.\exp\left\{-\frac{[k\Delta t - \tau_{\mathrm{D,NU}}(k)]^2}{(\Delta t)^2}\right\}\right) / \left\{2(N-k-1)\left[\sum_{i=2}^{N-1}(x_i-\bar{x})^2\cdot 2 + (x_1-\bar{x})^2\cdot 1 + (x_N-\bar{x})^2\cdot 1\right]\right\} \qquad \text{(A8)} \\
\approx {} & \frac{N-1}{N-k-1}\frac{\sum_{i=1}^{N-k}(x_i-\bar{x})(x_{i+k}-\bar{x})\exp\left\{-\frac{[k\Delta t-\tau_{\mathrm{D,NU}}(k)]^2}{(\Delta t)^2}\right\}}{\sum_{i=1}^{N}(x_i-\bar{x})^2}, \quad k \in \mathbb{N}, k \le N-10.
\end{aligned}
$$

A natural choice that ensures consistency [i.e., that Equation (A8) reduces to Equation (A6) under uniform sampling] is $\tau_{\mathrm{D,NU}}(k)$ should reduce to $k\Delta t$ under uniform sampling. Therefore, $\tau_{\mathrm{D,NU}}(k)$ [i.e. Equation (1) in the main text] is

given by

$$\tau_{\mathrm{D,NU}}(k) = \overline{t_{i+k} - t_i} = \frac{1}{N-k}\sum_{i=1}^{N-k}(t_{i+k} - t_i). \tag{A9}$$

This definition minimizes the expected value of the residual misalignment $t_i - t_{i+k} + \tau_{\mathrm{D,NU}}(k)$ to zero, thereby providing the best overall temporal alignment between the series $\{t_i + \tau_{\mathrm{D,NU}}(k) | \, i = 1, 2, \cdots, \quad N-k\}$ and $\{t_i | \, i = k+1, k+2, \cdots, N\}$:

$$\begin{aligned} E[t_i - t_{i+k} + \tau_{\mathrm{D,NU}}(k)] &= E\left[t_i - t_{i+k} + \frac{1}{N-k}\sum_{i=1}^{N-k}(t_{i+k} - t_i)\right] \\ &= E\left(t_i - \frac{1}{N-k}\sum_{i=1}^{N-k} t_i\right) - E\left(t_{i+k} - \frac{1}{N-k}\sum_{i=1}^{N-k} t_{i+k}\right) \\ &= E(t_i - \bar{t_i}) - E(t_{i+k} - \bar{t_{i+k}}) = 0. \end{aligned} \tag{A10}$$

Here we exploit the fact that the mean of a stationary series is time-invariant.

Substituting Equation (A9) into Equation (A7) leads to the final compact form of the NUACF presented in the main text [i.e. Equation (2)]:

$$\mathrm{acf}_{\mathrm{D,NU}}(k) = \frac{h_{N,1}}{h_{N-k,1} + h_{N,k+1}} \frac{\sum_{i=1}^{N-k}(x_i - \bar{x})(x_{i+k} - \bar{x}) H_i^{(2)} w_i}{\sum_{i=1}^{N}(x_i - \bar{x})^2 H_i^{(1)}}, \quad k \in \mathbb{N}, k \le N - 10, \tag{A11}$$

where we define $h_{m,n} = t_m - t_n$ for conciseness. The discrete weight factors $H_i^{(1)}$ and $H_i^{(2)}$ are derived via the trapezoidal rule. Along with the misalignment weight w_i in this final form, they are defined as follows:

$$H_i^{(1)} = \begin{cases} h_{i+1,i}, & i = 1, \\ h_{i+1,i-1}, & 1 < i < N, \\ h_{i,i-1}, & i = N, \end{cases} \tag{A12}$$

$$\begin{aligned} H_i^{(2)} &= \begin{cases} h_{i+1,i} + h_{i+k+1,i+k}, & i = 1, \\ h_{i+1,i-1} + h_{i+k+1,i+k-1}, & 1 < i < N-k, \\ h_{i,i-1} + h_{i+k,i+k-1}, & i = N-k, \end{cases} \\ &= \begin{cases} H_i^{(1)} + H_{i+k}^{(1)} - h_{i+k,i+k-1}, & i = 1, \\ H_i^{(1)} + H_{i+k}^{(1)}, & 1 < i < N-k, \\ H_i^{(1)} + H_{i+k}^{(1)} - h_{i+1,i}, & i = N-k, \end{cases} \end{aligned} \tag{A13}$$

$$w_i = \exp\left[-\frac{(N-1)^2\left(h_{i+k,i} - \overline{h_{i+k,i}}\right)^2}{h_{N,1}^2}\right]. \tag{A14}$$

Given an observation-number lag k, Equations (A9) and (A11) directly provide the corresponding physical time delay $\tau_{\mathrm{D,NU}}(k)$ and the NUACF value $\mathrm{acf}_{\mathrm{D,NU}}(k)$. This formulation is self-consistent in that it degenerates exactly to the standard sample ACF [Equation (A6)] and its associated time delay when applied to uniformly sampled data.

B. CONFIDENCE INTERVALS FOR THE NONUNIFORM AUTOCORRELATION FUNCTION

We now consider the confidence intervals of our NUACF. Specifically, to determine whether a peak in the NUACF is statistically meaningful, we need to assess if such a peak arises from random fluctuations of the data. The core idea is to set up a white noise sequence (i.e. a random signal with a flat power spectrum across all frequencies) and derive the distribution of the NUACF values at different lags k. As noted in Section 1, real observational sampling cannot be adequately described by an ideal Poisson process. Consequently, the NUACF is model-independent by construction. This property should naturally extend to its confidence intervals, a point that will be demonstrated by the following theoretical derivation.

We begin by reviewing the standard ACF for a uniformly sampled series. For a white noise sequence, we expect $\mathrm{acf}_{\mathrm{D,U}}(k) = 0$ in Equation (A6), since x_i and x_{i+k} are independent. In practice, due to finite sample size, the calculated $\mathrm{acf}_{\mathrm{D,U}}(k)$ exhibits fluctuations around zero. From the Central Limit Theorem (CLT) for independent and identically distributed (i.i.d.) variables, we have

$$\frac{1}{N-k}\sum_{i=1}^{N-k}(x_i-\bar{x})(x_{i+k}-\bar{x}) \sim \mathcal{N}\left\{E\left[(x_i-\bar{x})(x_{i+k}-\bar{x})\right], \frac{D\left[(x_i-\bar{x})(x_{i+k}-\bar{x})\right]}{N-k}\right\}, \tag{B1}$$

where $\mathcal{N}\left(\mu_{\mathcal{N}}, \sigma_{\mathcal{N}}^2\right)$ denotes a normal distribution. Leveraging the independence and stationarity of $\{x_i | \, i = 1, 2, \cdots, N\}$, we have

$$E\left[(x_i-\bar{x})(x_{i+k}-\bar{x})\right] = E(x_i-\bar{x})\,E(x_{i+k}-\bar{x}) = 0, \tag{B2}$$

$$\begin{aligned} D\left[(x_i-\bar{x})(x_{i+k}-\bar{x})\right] &= E\left[(x_i-\bar{x})^2(x_{i+k}-\bar{x})^2\right] - \left\{E\left[(x_i-\bar{x})(x_{i+k}-\bar{x})\right]\right\}^2 \\ &= E\left[(x_i-\bar{x})^2\right]E\left[(x_{i+k}-\bar{x})^2\right] \\ &= \left\{D(x_i-\bar{x}) + \left[E(x_i-\bar{x})\right]^2\right\}\left\{D(x_{i+k}-\bar{x}) + \left[E(x_{i+k}-\bar{x})\right]^2\right\} \\ &= D(x_i-\bar{x})\,D(x_{i+k}-\bar{x}) = \sigma_{\mathrm{D,U}}^4. \end{aligned} \tag{B3}$$

Substituting Equations (B2) and (B3) into (B1) yields

$$\frac{1}{N-k}\sum_{i=1}^{N-k}(x_i-\bar{x})(x_{i+k}-\bar{x}) \sim \mathcal{N}\left(0, \frac{\sigma_{\mathrm{D,U}}^4}{N-k}\right). \tag{B4}$$

Combining Equation (B4) with Equation (A6) and using the approximation $\frac{1}{N}\sum_{i=1}^{N}(x_i-\bar{x})^2 \approx \sigma_{\mathrm{D,U}}^2$, we obtain the distribution for the ACF value of a white-noise, uniformly sampled series:

$$\mathrm{acf}_{\mathrm{D,U}}^{\mathrm{noise}}(k) \sim \mathcal{N}\left(0, \frac{1}{N-k}\right). \tag{B5}$$

For a normal distribution $\mathcal{N}\left(\mu_{\mathcal{N}}, \sigma_{\mathcal{N}}^2\right)$, the $100\,(1-\alpha)\,\%$ confidence interval is given by $\left[\mu_{\mathcal{N}} - z_{\alpha/2}\sigma_{\mathcal{N}},\ \ \mu_{\mathcal{N}} + z_{\alpha/2}\sigma_{\mathcal{N}}\right]$, where $z_{\alpha/2}$ is the critical value from the standard normal distribution, satisfying $P\left(Z > \ z_{\alpha/2}\right) = \frac{\alpha}{2}$ for $Z \sim \mathcal{N}(0,1)$. Thus, the confidence interval for the standard sample ACF is

$$\mathrm{acf}_{\mathrm{D,U}}^{\mathrm{noise}}(k) \in \left[-\frac{z_{\alpha/2}}{\sqrt{N-k}}, \frac{z_{\alpha/2}}{\sqrt{N-k}}\right]. \tag{B6}$$

This interval describes the range within which the ACF values of a purely white-noise, uniformly sampled series are expected to lie. Therefore, ACF values falling outside this interval for a real uniform time series can be considered

statistically significant. For consistency with common terminology, we will still refer to Equation (B6) as a "confidence interval," while noting that it actually defines a rejection region against ACF fluctuations arising from noise.

We extend this reasoning to derive the confidence intervals of our NUACF. A key quantity is $h_{i+k,i} = t_{i+k} - t_i$. If the sampling times are generated by a Poisson process, the intervals $h_{m,m-1}$ follow an exponential distribution. Consequently, $h_{i+k,i}$, being the sum of k such intervals, follows an Erlang distribution (a distribution widely used in queueing theory) with the probability density expressed as

$$f_{\text{Erlang}}\left(h_{i+k,i}\right) = \frac{\lambda^k}{(k-1)!} h_{i+k,i}^{k-1} \exp\left(-\lambda h_{i+k,i}\right), \quad h_{i+k,i} > 0. \tag{B7}$$

The mean and variance of the Erlang distribution are given by:

$$E\left(h_{i+k,i}\right) = \frac{k}{\lambda} = \overline{h_{i+k,i}} = \frac{1}{N-k} \sum_{i=1}^{N-k} h_{i+k,i}, \tag{B8}$$

$$D\left(h_{i+k,i}\right) = \frac{k}{\lambda^2} = \frac{1}{N-k} \sum_{i=1}^{N-k} \left(h_{i+k,i} - \overline{h_{i+k,i}}\right)^2. \tag{B9}$$

The Erlang distribution reduces to the exponential distribution when $k = 1$. For the case $k = 1$, Equation (B8) and the stationarity of the series yield

$$\frac{1}{\lambda} = \frac{1}{N-1} \sum_{i=1}^{N-1} h_{i+1,i} = \frac{h_{N,1}}{N-1}, \tag{B10}$$

where λ is the event rate of the Poisson process, which is assumed to be constant.

If we extend the observed time series by a preceding instant t_0 and a following instant t_{N+1}, Equation (A11) can be rewritten as

$$\text{acf}_{\text{D,NU}}\left(k\right) = \frac{h_{N,1}}{h_{N-k,1} + h_{N,k+1}} \frac{\sum_{i=1}^{N-k} \left(x_i - \bar{x}\right)\left(x_{i+k} - \bar{x}\right)\left(h_{i+1,i-1} + h_{i+k+1,i+k-1}\right) \exp\left[-\frac{(N-1)^2\left(h_{i+k,i} - \overline{h_{i+k,i}}\right)^2}{h_{N,1}^2}\right]}{\sum_{i=1}^{N} \left(x_i - \bar{x}\right)^2 h_{i+1,i-1}}. \tag{B11}$$

Substituting Equations (B8) and (B10) into (B11), we get

$$\text{acf}_{\text{D,NU}}\left(k\right) = \frac{h_{N,1}}{h_{N-k,1} + h_{N,k+1}} \frac{\sum_{i=1}^{N-k} \left(x_i - \bar{x}\right)\left(x_{i+k} - \bar{x}\right)\left(h_{i+1,i-1} + h_{i+k+1,i+k-1}\right) \exp\left[-\left(\lambda h_{i+k,i} - k\right)^2\right]}{\sum_{i=1}^{N} \left(x_i - \bar{x}\right)^2 h_{i+1,i-1}}. \tag{B12}$$

Let us define $A_i = \left(x_i - \bar{x}\right)\left(x_{i+k} - \bar{x}\right)\left(h_{i+1,i-1} + h_{i+k+1,i+k-1}\right) \exp\left[-\left(\lambda h_{i+k,i} - k\right)^2\right]$. From the CLT for i.i.d. variables, we have

$$\sum_{i=1}^{N-k} A_i \sim \mathcal{N}\left[\left(N-k\right) E\left(A_i\right), \left(N-k\right) D\left(A_i\right)\right]. \tag{B13}$$

Given the independence and stationarity of $\{x_i | \, i = 1, 2, \cdots, N\}$, we obtain

$$\begin{aligned} E\left(A_i\right) &= E\left\{\left(x_i - \bar{x}\right)\left(x_{i+k} - \bar{x}\right)\left(h_{i+1,i-1} + h_{i+k+1,i+k-1}\right) \exp\left[-\left(\lambda h_{i+k,i} - k\right)^2\right]\right\} \\ &= E\left(x_i - \bar{x}\right) E\left(x_{i+k} - \bar{x}\right) E\left\{\left(h_{i+1,i-1} + h_{i+k+1,i+k-1}\right) \exp\left[-\left(\lambda h_{i+k,i} - k\right)^2\right]\right\} \\ &= 0 \cdot 0 \cdot E\left\{\left(h_{i+1,i-1} + h_{i+k+1,i+k-1}\right) \exp\left[-\left(\lambda h_{i+k,i} - k\right)^2\right]\right\} = 0, \end{aligned} \tag{B14}$$

$$\begin{aligned} D\left(A_i\right) &= E\left(A_i^2\right) - \left[E\left(A_i\right)\right]^2 \\ &= E\left[\left(x_i-\bar{x}\right)^2\right]\ E\left[\left(x_{i+k}-\bar{x}\right)^2\right] E\left[\left(h_{i+1,i-1}+h_{i+k+1,i+k-1}\right)^2\right] E\left\{\exp\left[-2\left(\lambda h_{i+k,i}-k\right)^2\right]\right\} \\ &= D\left(x_i-\bar{x}\right) D\left(x_{i+k}-\bar{x}\right) E\left[\left(h_{i+1,i-1}+h_{i+k+1,i+k-1}\right)^2\right] E\left\{\exp\left[-2\left(\lambda h_{i+k,i}-k\right)^2\right]\right\} \\ &= \sigma_{\mathrm{D,U}}^4 E\left[\left(h_{i+1,i-1}+h_{i+k+1,i+k-1}\right)^2\right] E\left\{\exp\left[-2\left(\lambda h_{i+k,i}-k\right)^2\right]\right\}. \end{aligned} \tag{B15}$$

Employing Equations (B8) and (B9), the expectation $E\left[\left(h_{i+1,i-1}+h_{i+k+1,i+k-1}\right)^2\right]$ in Equation (B15) is evaluated as:

$$\begin{aligned} E\left[\left(h_{i+1,i-1}+h_{i+k+1,i+k-1}\right)^2\right] &= D\left(h_{i+1,i-1}+h_{i+k+1,i+k-1}\right) + \left[E\left(h_{i+1,i-1}+h_{i+k+1,i+k-1}\right)\right]^2 \\ &= D\left(h_{i+1,i-1}\right) + D\left(h_{i+k+1,i+k-1}\right) + \left[E\left(h_{i+1,i-1}\right)+E\left(h_{i+k+1,i+k-1}\right)\right]^2 = \frac{20}{\lambda^2}. \end{aligned} \tag{B16}$$

The expectation $E\left\{\exp\left[-2\left(\lambda h_{i+k,i}-k\right)^2\right]\right\}$ in Equation (B15) is computed by substituting Equation (B7) and letting $g=\lambda h_{i+k,i}-\left(k-\frac{1}{4}\right)$:

$$\begin{aligned} E\left\{\exp\left[-2\left(\lambda h_{i+k,i}-k\right)^2\right]\right\} &= \int_0^\infty \exp\left[-2\left(\lambda h_{i+k,i}-k\right)^2\right]\frac{\lambda^k}{(k-1)!}h_{i+k,i}^{k-1}\exp\left(-\lambda h_{i+k,i}\right)\mathrm{d}h_{i+k,i} \\ &= \frac{\exp\left(-k+\frac{1}{8}\right)}{(k-1)!}\int_{-k+\frac{1}{4}}^\infty \left(g+k-\frac{1}{4}\right)^{k-1}\exp\left(-2g^2\right)\mathrm{d}g \\ &= \frac{\exp\left(-k+\frac{1}{8}\right)}{(k-1)!}\int_{-k+\frac{1}{4}}^\infty \left[\sum_{r=0}^{k-1}\frac{(k-1)!}{r!\,(k-r-1)!}g^{k-r-1}\left(k-\frac{1}{4}\right)^r\right]\exp\left(-2g^2\right)\mathrm{d}g \\ &= \exp\left(-k+\frac{1}{8}\right)\sum_{r=0}^{k-1}\left[\frac{\left(k-\frac{1}{4}\right)^r}{r!\,(k-r-1)!}\int_{-k+\frac{1}{4}}^\infty g^{k-r-1}\exp\left(-2g^2\right)\mathrm{d}g\right]. \end{aligned} \tag{B17}$$

The integral can be expressed in terms of the Gamma function $\Gamma(m)=\int_0^\infty a^{m-1}\mathrm{e}^{-a}\mathrm{d}a$ and the lower incomplete Gamma function $\gamma(m,n)=\int_0^n a^{m-1}\mathrm{e}^{-a}\mathrm{d}a$:

$$\begin{aligned} \int_{-k+\frac{1}{4}}^\infty g^{k-r-1}\exp\left(-2g^2\right)\mathrm{d}g &= \int_0^\infty g^{k-r-1}\exp\left(-2g^2\right)\mathrm{d}g + \int_{-k+\frac{1}{4}}^0 g^{k-r-1}\exp\left(-2g^2\right)\mathrm{d}g \\ &= 2^{-\frac{k-r+2}{2}}\left[\int_0^\infty \left(2g^2\right)^{\frac{k-r-2}{2}}\exp\left(-2g^2\right)\mathrm{d}\left(2g^2\right)\right. \\ &\quad \left. -(-1)^{k-r}\int_0^{2\left(k-\frac{1}{4}\right)^2}\left(2g^2\right)^{\frac{k-r-2}{2}}\exp\left(-2g^2\right)\mathrm{d}\left(2g^2\right)\right] \\ &= 2^{-\frac{k-r+2}{2}}\left\{\Gamma\left(\frac{k-r}{2}\right)-(-1)^{k-r}\gamma\left[\frac{k-r}{2},2\left(k-\frac{1}{4}\right)^2\right]\right\}. \end{aligned} \tag{B18}$$

Substituting Equations (B16)–(B18) into (B15), we have

$$D\left(A_i\right)=\frac{20}{\lambda^2}\sigma_{\mathrm{D,U}}^4\exp\left(-k+\frac{1}{8}\right)\sum_{r=0}^{k-1}\left(2^{-\frac{k-r+2}{2}}\frac{\left(k-\frac{1}{4}\right)^r}{r!\,(k-r-1)!}\left\{\Gamma\left(\frac{k-r}{2}\right)-(-1)^{k-r}\gamma\left[\frac{k-r}{2},2\left(k-\frac{1}{4}\right)^2\right]\right\}\right) \tag{B19}$$

Inserting Equations (B14) and (B19) into (B13), and combining the results of Equations (A2), (B10) and (B12), we obtain the distribution of the NUACF value under the white noise hypothesis:

$$\begin{aligned} \mathrm{acf}_{\mathrm{D,NU}}^{\mathrm{noise}}(k) \sim \mathcal{N}\left[0,5\frac{N-k}{(N-1)^2}\frac{h_{N,1}^2}{\left(h_{N-k,1}+h_{N,k+1}\right)^2}\frac{\sigma_{\mathrm{D,U}}^4}{\sigma_{\mathrm{D,NU}}^4}\exp\left(-k+\frac{1}{8}\right)\right. \\ \left.\sum_{r=0}^{k-1}\left(2^{-\frac{k-r+2}{2}}\frac{\left(k-\frac{1}{4}\right)^r}{r!\,(k-r-1)!}\left\{\Gamma\left(\frac{k-r}{2}\right)-(-1)^{k-r}\gamma\left[\frac{k-r}{2},2\left(k-\frac{1}{4}\right)^2\right]\right\}\right)\right]. \end{aligned} \tag{B20}$$

Hence, the $100\,(1-\alpha)\,\%$ confidence interval for the NUACF [i.e. Equation (3) in the main text] is

$$\mathrm{acf}^{\mathrm{noise}}_{\mathrm{D,NU}}\,(k) \in \left[-z_{\alpha/2}V\,(k)\,, z_{\alpha/2}V\,(k)\right], \tag{B21}$$

where $V\,(k)$ is the square root of the variance expression in Equation (B20), i.e., the right-hand side of Equation (B20) is treated as $\mathcal{N}\left\{0, [V\,(k)]^2\right\}$. Unlike the uniform-sampling case, the NUACF confidence interval depends explicitly on the observed time stamps $\{t_i|\, i = 1, 2, \cdots, N\}$. Furthermore, while the NUACF itself degenerates to the standard sample ACF under uniform sampling, its confidence interval [Equation (B21)] does not degenerate to Equation (B6). This is because its derivation employs the Erlang distribution for temporal intervals, which does not collapse to a distribution described by the Dirac function under uniform sampling.

To avoid numerical overflow and ensure stability, $V\,(k)$ can be calculated using

$$\begin{aligned} V\,(k) = \Bigg[& 5\frac{N-k}{(N-1)^2}\frac{h_{N,1}^2}{\left(h_{N-k,1}+h_{N,k+1}\right)^2}\frac{\sigma_{\mathrm{D,U}}^4}{\sigma_{\mathrm{D,NU}}^4} \\ & \sum_{r=0}^{k-1}\left(\exp\left\{\frac{1}{8}-k-\frac{k-r+2}{2}\ln 2 + r\ln\left(k-\frac{1}{4}\right) - \ln\left[\Gamma\,(r+1)\right] - \ln\left[\Gamma\,(k+r)\right]\right\}\right. \\ & \left.\left\{\Gamma\left(\frac{k-r}{2}\right) - (-1)^{k-r}\,\gamma\left[\frac{k-r}{2}, 2\left(k-\frac{1}{4}\right)^2\right]\right\}\right)\Bigg]^{0.5}. \end{aligned} \tag{B22}$$

The Gamma functions $\Gamma\,(m)$ and $\ln\left[\Gamma\,(m)\right]$ can be computed via `scipy.special.gamma` and `scipy.special.gammaln`, respectively. The lower incomplete gamma function $\gamma\,(m, n)$ is obtained using `scipy.special.gammainc`.

However, since real observation times are fixed and not strictly Poissonian, a more practical approach is to derive the confidence interval via MC simulations of white-noise fluxes at the fixed observation times. As detailed in the main text (see the discussion accompanying Figures 3 & 4), while the theoretical derivation provides a useful guide, the fixed-time MC calculation proves more reliable for practical analysis. Consequently, we employ MC-based NUACF confidence intervals for all analyses in this work.

C. UNCERTAINTY OF TIME DELAYS

When a significant peak or trough is identified through our NUACF method, determining the corresponding time delay and its uncertainty becomes crucial. The uncertainty of time delay stems from two independent sources: flux measurement errors and temporal irregularity in the sampling. Traditional methods, such as the interpolated/resampled ACF or the time-delay-binned DCF typically assess the contribution from flux errors through MC simulations. However, they inherently fail to account for the uncertainty introduced by the temporal irregularity. These conventional approaches suppress the impact of irregular sampling by introducing artificial regularization, yet they cannot adequately incorporate the associated biases into an effective error budget.

Our NUACF framework, in contrast, naturally accommodates a full uncertainty estimation. We first address the error originating from temporal irregularity. Based on Equation (A9) and the CLT, we have:

$$\tau_{\mathrm{D,NU}}\,(k) = \overline{h_{i+k,i}} = \frac{1}{N-k}\sum_{i=1}^{N-k} h_{i+k,i} \sim \mathcal{N}\left[E\left(h_{i+k,i}\right), \frac{D\left(h_{i+k,i}\right)}{N-k}\right]. \tag{C1}$$

Substituting the expectation and variance of $h_{i+k,i}$ into Equation (C1) yields

$$\tau_{\mathrm{D,NU}}\,(k) \sim \mathcal{N}\left[\overline{h_{i+k,i}}, \frac{1}{(N-k)^2}\sum_{i=1}^{N-k}\left(h_{i+k,i}-\overline{h_{i+k,i}}\right)^2\right]. \tag{C2}$$

Consequently, the uncertainty in $\tau_{\mathrm{D,NU}}\,(k)$ due to temporal irregularity [i.e. Equation (4) in the main text] is

$$\varepsilon_t\left[\tau_{\mathrm{D,NU}}\,(k)\right] = \frac{1}{N-k}\sqrt{\sum_{i=1}^{N-k}\left(h_{i+k,i}-\overline{h_{i+k,i}}\right)^2}. \tag{C3}$$

Next, we consider the uncertainty propagated from flux measurement errors. If, within the error bounds of each flux measurement, a new flux value is randomly generated to create a new light curve, the estimated lag k corresponding to the same underlying physical time delay may fluctuate. This leads to a distribution of estimated time delays, representing the error contribution from flux uncertainties. To combine this with the temporal irregularity error, we employ MC simulations. The procedure is as follows: in each simulation run, a new signal sequence is generated by randomizing the fluxes based on their central values and errors. The NUACF and its confidence band are then used to locate significant peaks, and Equation (C3) is applied to compute the temporal irregularity error ε_t for the time delay associated with each peak. After completing all runs, for the φ-th underlying time delay (corresponding to the φ-th significant NUACF peak, P_φ), we obtain ensembles of time delay estimates $\left\{ \tau_{\mathrm{D,NU}}^{(\xi)}\left(k_{\mathrm{P}_\varphi}\right) \middle| \xi = 1, 2, \cdots, S \right\}$ and their associated temporal irregularity errors $\left\{ \varepsilon_t \left[\tau_{\mathrm{D,NU}}^{(\xi)}\left(k_{\mathrm{P}_\varphi}\right) \right] \middle| \xi = 1, 2, \cdots, S \right\}$.

The uncertainty for the sample estimate of the φ-th underlying time delay [i.e. Equation (5) in the main text] is then given by:

$$\varepsilon_{\mathrm{total}}\left[\tau_{\mathrm{D,NU}}\left(k_{\mathrm{P}_\varphi}\right)\right] = \sqrt{\frac{\sum_\xi \left[\tau_{\mathrm{D,NU}}^{(\xi)}\left(k_{\mathrm{P}_\varphi}\right) - \overline{\tau_{\mathrm{D,NU}}^{(\xi)}\left(k_{\mathrm{P}_\varphi}\right)}\right]^2}{S\left(S-1\right)} + \overline{\left\{\varepsilon_t\left[\tau_{\mathrm{D,NU}}^{(\xi)}\left(k_{\mathrm{P}_\varphi}\right)\right]\right\}^2}}. \tag{C4}$$

Here, $\overline{\tau_{\mathrm{D,NU}}^{(\xi)}\left(k_{\mathrm{P}_\varphi}\right)}$ serves as the final sample estimate for the φ-th time delay, and Equation (C4) represents its complete uncertainty. Three important points should be noted in this process:

(1) Since the observation times are fixed, the MC-based NUACF confidence intervals need to be prepared only once for the entire analysis and can be reused in each simulation run for the complete error calculation, eliminating the need for nested MC simulations.

(2) As repetitive variability patterns may occur, multiple significant NUACF peaks can be present. After all simulation runs, the time delays corresponding to all identified significant peaks can be plotted in a histogram. The clustering in this histogram (e.g., a Gaussian distribution around a specific underlying time delay) can then be used to group delays belonging to the same physical time delay.

(3) Increasing the confidence level of the NUACF confidence interval can help filter out less significant peaks that exhibit poor clustering in the simulations, thereby focusing the analysis on robustly detected time delays.

D. EXTENDING TO THE NONUNIFORM CROSS-CORRELATION FUNCTION

Building upon the NUACF framework, we now introduce the NUCCF to quantify the similarity between two irregularly sampled time series, $\{(x_i, t_i^x) | \, i = 1, 2, \cdots, N\}$ and $\{(y_i, t_i^y) | \, i = 1, 2, \cdots, M\}$. As a foundation, for uniformly sampled data, the standard sample CCF is given by

$$\mathrm{ccf}_{\mathrm{D,U}}\left(k\right) = \frac{\sqrt{NM}}{i_{\max} - i_{\min} + 1} \frac{\sum_{i=i_{\min}}^{i_{\max}} \left(x_i - \bar{x}\right)\left(y_{i+k} - \bar{y}\right)}{\sqrt{\sum_{i=1}^{N}\left(x_i - \bar{x}\right)^2 \sum_{i=1}^{M}\left(y_i - \bar{y}\right)^2}}, \quad k \in \mathbb{Z}, -\left(N-10\right) \leq k \leq M - 10, \tag{D1}$$

where $i_{\min} = \max\left(1, 1-k\right)$ and $i_{\max} = \min\left(N, M-k\right)$.

Following the same logic used to extend the sample ACF from uniform to nonuniform sampling [Equations (A6)–(A14)], we generalize Equation (D1) to obtain the NUCCF:

$$
\begin{aligned}
\mathrm{ccf}_{\mathrm{D,NU}}(k) = & \left[\left\{1/\left[\frac{t^x_{i_{\max}}+\tau^{xy}_{\mathrm{D,NU}}(k)+t^y_{i_{\max}+k}}{2}-\frac{t^x_{i_{\min}}+\tau^{xy}_{\mathrm{D,NU}}(k)+t^y_{i_{\min}+k}}{2}\right]\right\}\right. \\
& \left(\sum_{i=i_{\min}+1}^{i_{\max}-1}(x_i-\bar{x})(y_{i+k}-\bar{y})\left\{\frac{1}{2}\left[\frac{t^x_{i+1}+\tau^{xy}_{\mathrm{D,NU}}(k)+t^y_{i+k+1}}{2}-\frac{t^x_{i-1}+\tau^{xy}_{\mathrm{D,NU}}(k)+t^y_{i+k-1}}{2}\right]\right\}w_i\right. \\
& +(x_{i_{\min}}-\bar{x})(y_{i_{\min}+k}-\bar{y})\left\{\frac{1}{2}\left[\frac{t^x_{i_{\min}+1}+\tau^{xy}_{\mathrm{D,NU}}(k)+t^y_{i_{\min}+k+1}}{2}-\frac{t^x_{i_{\min}}+\tau^{xy}_{\mathrm{D,NU}}(k)+t^y_{i_{\min}+k}}{2}\right]\right\}w_{i_{\min}} \\
& \left.\left.+(x_{i_{\max}}-\bar{x})(y_{i_{\max}+k}-\bar{y})\left\{\frac{1}{2}\left[\frac{t^x_{i_{\max}}+\tau^{xy}_{\mathrm{D,NU}}(k)+t^y_{i_{\max}+k}}{2}-\frac{t^x_{i_{\max}-1}+\tau^{xy}_{\mathrm{D,NU}}(k)+t^y_{i_{\max}+k-1}}{2}\right]\right\}w_{i_{\max}}\right)\right], \\
& /\left[\left(\left[1/\left(t^x_N-t^x_1\right)\right]\left\{\sum_{i=2}^{N-1}(x_i-\bar{x})^2\left[\frac{1}{2}\left(t^x_{i+1}-t^x_{i-1}\right)\right]+(x_1-\bar{x})^2\left[\frac{1}{2}\left(t^x_2-t^x_1\right)\right]+(x_N-\bar{x})^2\left[\frac{1}{2}\left(t^x_N-t^x_{N-1}\right)\right]\right\}\right)^{0.5}\right. \\
& \left.\left(\left[1/\left(t^y_M-t^y_1\right)\right]\left\{\sum_{i=2}^{M-1}(y_i-\bar{y})^2\left[\frac{1}{2}\left(t^y_{i+1}-t^y_{i-1}\right)\right]+(y_1-\bar{y})^2\left[\frac{1}{2}\left(t^y_2-t^y_1\right)\right]+(y_M-\bar{y})^2\left[\frac{1}{2}\left(t^y_M-t^y_{M-1}\right)\right]\right\}\right)^{0.5}\right] \qquad \text{(D2)} \\
= & \left(\left[\left(t^x_N-t^x_1\right)\left(t^y_M-t^y_1\right)\right]^{0.5}\left\{\sum_{i=i_{\min}+1}^{i_{\max}-1}(x_i-\bar{x})(y_{i+k}-\bar{y})\left[\left(t^x_{i+1}-t^x_{i-1}\right)+\left(t^y_{i+k+1}-t^y_{i+k-1}\right)\right]w_i\right. \\
& +(x_{i_{\min}}-\bar{x})(y_{i_{\min}+k}-\bar{y})\left[\left(t^x_{i_{\min}+1}-t^x_{i_{\min}}\right)+\left(t^y_{i_{\min}+k+1}-t^y_{i_{\min}+k}\right)\right]w_{i_{\min}} \\
& \left.+(x_{i_{\max}}-\bar{x})(y_{i_{\max}+k}-\bar{y})\left[\left(t^x_{i_{\max}}-t^x_{i_{\max}-1}\right)+\left(t^y_{i_{\max}+k}-t^y_{i_{\max}+k-1}\right)\right]w_{i_{\max}}\right\}) \\
& /\left(\left[\left(t^x_{i_{\max}}-t^x_{i_{\min}}\right)+\left(t^y_{i_{\max}+k}-t^y_{i_{\min}+k}\right)\right]\left\{\left[\sum_{i=2}^{N-1}(x_i-\bar{x})^2\left(t^x_{i+1}-t^x_{i-1}\right)+(x_1-\bar{x})^2\left(t^x_2-t^x_1\right)+(x_N-\bar{x})^2\left(t^x_N-t^x_{N-1}\right)\right]\right. \\
& \left.\left.\left[\sum_{i=2}^{M-1}(y_i-\bar{y})^2\left(t^y_{i+1}-t^y_{i-1}\right)+(y_1-\bar{y})^2\left(t^y_2-t^y_1\right)+(y_M-\bar{y})^2\left(t^y_M-t^y_{M-1}\right)\right]\right\}^{0.5}\right), \\
& k\in\mathbb{Z}, -(N-10)\le k\le M-10,
\end{aligned}
$$

where $w_i=\exp\left\{-\frac{(N-1)(M-1)\left[t^x_i-t^y_{i+k}+\tau^{xy}_{\mathrm{D,NU}}(k)\right]^2}{\left(t^x_N-t^x_1\right)\left(t^y_M-t^y_1\right)}\right\}$ and $\tau^{xy}_{\mathrm{D,NU}}(k)$ denotes the time delay at lag k. When the sampling is uniform, with constant intervals Δt^x for series $\{x_i\}$ and Δt^y for series $\{y_i\}$, Equation (D2) simplifies to

$$
\begin{aligned}
\mathrm{ccf}_{\mathrm{D,NU\to U}}(k) = & \left(\left[(N-1)\Delta t^x(M-1)\Delta t^y\right]^{0.5}\left\{\sum_{i=i_{\min}+1}^{i_{\max}-1}(x_i-\bar{x})(y_{i+k}-\bar{y})\left[2\left(\Delta t^x+\Delta t^y\right)\right]w_i\right. \\
& \left.+(x_{i_{\min}}-\bar{x})(y_{i_{\min}+k}-\bar{y})\left(\Delta t^x+\Delta t^y\right)w_{i_{\min}}+(x_{i_{\max}}-\bar{x})(y_{i_{\max}+k}-\bar{y})\left(\Delta t^x+\Delta t^y\right)w_{i_{\max}}\right\}) \\
& /\left(\left[(i_{\max}-i_{\min})\left(\Delta t^x+\Delta t^y\right)\right]\left\{\left[\sum_{i=2}^{N-1}(x_i-\bar{x})^2\left(2\Delta t^x\right)+(x_1-\bar{x})^2\Delta t^x+(x_N-\bar{x})^2\Delta t^x\right]\right. \\
& \left.\left.\left[\sum_{i=2}^{M-1}(y_i-\bar{y})^2\left(2\Delta t^y\right)+(y_1-\bar{y})^2\Delta t^y+(y_M-\bar{y})^2\Delta t^y\right]\right\}^{0.5}\right) \qquad \text{(D3)} \\
\approx & \frac{\sqrt{(N-1)(M-1)}}{i_{\max}-i_{\min}}\frac{\sum_{i=i_{\min}}^{i_{\max}}(x_i-\bar{x})(y_{i+k}-\bar{y})\exp\left\{-\frac{\left[t^x_i-t^y_{i+k}+\tau^{xy}_{\mathrm{D,NU}}(k)\right]^2}{\Delta t^x\Delta t^y}\right\}}{\sqrt{\sum_{i=1}^{N}(x_i-\bar{x})^2\sum_{i=1}^{M}(y_i-\bar{y})^2}}, \\
& k\in\mathbb{Z}, -(N-10)\le k\le M-10.
\end{aligned}
$$

To ensure that Equation (D3) degenerates exactly to the uniform sampling form Equation (D1), it is natural to define the time delay $\tau^{xy}_{\mathrm{D,NU}}(k)$ as the average temporal offset of the matched pairs [i.e. Equation (7) in the main text]:

$$\tau^{xy}_{\mathrm{D,NU}}(k) = \overline{t^y_{i+k} - t^x_i} = \frac{1}{i_{\max} - i_{\min} + 1} \sum_{i=i_{\min}}^{i_{\max}} \left(t^y_{i+k} - t^x_i\right). \tag{D4}$$

This guarantees that the argument of the exponential in w_i has zero expectation,

$$\begin{aligned} E\left[t^x_i - t^y_{i+k} + \tau^{xy}_{\mathrm{D,NU}}(k)\right] &= E\left[t^x_i - t^y_{i+k} + \frac{1}{i_{\max} - i_{\min} + 1} \sum_{i=i_{\min}}^{i_{\max}} \left(t^y_{i+k} - t^x_i\right)\right] \\ &= E\left(t^x_i - \frac{1}{i_{\max} - i_{\min} + 1} \sum_{i=i_{\min}}^{i_{\max}} t^x_i\right) - E\left(t^y_{i+k} - \frac{1}{i_{\max} - i_{\min} + 1} \sum_{i=i_{\min}}^{i_{\max}} t^y_{i+k}\right) \\ &= E\left(t^x_i - \overline{t^x_i}\right) - E\left(t^y_{i+k} - \overline{t^y_{i+k}}\right) = 0, \end{aligned} \tag{D5}$$

thereby preserving the unbiased character of the estimator in the uniform sampling limit.

Substituting Equation (D4) into Equation (D2), we arrive at the final, self consistent form of the NUCCF that appears in the main text [i.e. Equation (6)]:

$$\mathrm{ccf}_{\mathrm{D,NU}}(k) = \frac{\sqrt{h^x_{N,1} h^y_{M,1}}}{h^x_{i_{\max},i_{\min}} + h^y_{i_{\max}+k,i_{\min}+k}} \frac{\sum_{i=i_{\min}}^{i_{\max}} (x_i - \bar{x})\left(y_{i+k} - \bar{y}\right) H^{xy,(2)}_i w^{xy}_i}{\sqrt{\sum_{i=1}^{N} (x_i - \bar{x})^2 H^{x,(1)}_i \sum_{i=1}^{M} \left(y_i - \bar{y}\right)^2 H^{y,(1)}_i}}, \tag{D6}$$
$$k \in \mathbb{Z}, -(N-10) \le k \le M - 10,$$

where $h^x_{m,n} = t^x_m - t^x_n$ and $h^y_{m,n} = t^y_m - t^y_n$. The discrete weight factors $H^{x,(1)}_i$, $H^{y,(1)}_i$ and $H^{xy,(2)}_i$, derived via the trapezoidal rule, along with the misalignment weight w^{xy}_i, are defined as:

$$H^{x,(1)}_i = \begin{cases} h^x_{i+1,i}, & i = 1, \\ h^x_{i+1,i-1}, & 1 < i < N, \\ h^x_{i,i-1}, & i = N, \end{cases} \tag{D7}$$

$$H^{y,(1)}_i = \begin{cases} h^y_{i+1,i}, & i = 1, \\ h^y_{i+1,i-1}, & 1 < i < M, \\ h^y_{i,i-1}, & i = M, \end{cases} \tag{D8}$$

$$H^{xy,(2)}_i = \begin{cases} h^x_{i+1,i} + h^y_{i+k+1,i+k}, & i = i_{\min}, \\ h^x_{i+1,i-1} + h^y_{i+k+1,i+k-1}, & i_{\min} < i < i_{\max}, \\ h^x_{i,i-1} + h^y_{i+k,i+k-1}, & i = i_{\max}, \end{cases} \tag{D9}$$

$$w^{xy}_i = \exp\left\{-\frac{(N-1)(M-1)\left[t^y_{i+k} - t^x_i - \overline{t^y_{i+k} - t^x_i}\right]^2}{\left(t^x_N - t^x_1\right)\left(t^y_M - t^y_1\right)}\right\}. \tag{D10}$$

The uncertainty in $\tau^{xy}_{\mathrm{D,NU}}(k)$ again comprises contributions from temporal irregularity and flux measurement errors. To estimate the uncertainty arising from temporal irregularity alone, we appeal to the Lindeberg-Feller CLT (Billingsley

1995) for independent, non-identically distributed variables, which yields the asymptotic distribution:

$$\tau_{\mathrm{D,NU}}^{xy}(k) \sim \mathcal{N}\left[\overline{t_{i+k}^{y}-t_{i}^{x}}, \frac{1}{(i_{\max}-i_{\min}+1)(i_{\max}-i_{\min})}\sum_{i=i_{\min}}^{i_{\max}}\left(t_{i+k}^{y}-t_{i}^{x}-\overline{t_{i+k}^{y}-t_{i}^{x}}\right)^{2}\right]. \tag{D11}$$

Consequently, the temporal irregularity error [i.e. Equation (9) in the main text] is

$$\varepsilon_{t}\left[\tau_{\mathrm{D,NU}}^{xy}(k)\right] = \sqrt{\frac{\sum_{i=i_{\min}}^{i_{\max}}\left(t_{i+k}^{y}-t_{i}^{x}-\overline{t_{i+k}^{y}-t_{i}^{x}}\right)^{2}}{(i_{\max}-i_{\min}+1)(i_{\max}-i_{\min})}}. \tag{D12}$$

The error component from flux measurement uncertainties is assessed via MC simulations, following a procedure analogous to that described for the NUACF in Appendix C. For each underlying time delay corresponding to a significant NUCCF peak P_{φ}, the ensemble of estimates $\left\{\tau_{\mathrm{D,NU}}^{xy,(\xi)}\left(k_{\mathrm{P}_{\varphi}}\right)\middle|\,\xi=1,2,\cdots,S\right\}$ and their associated temporal errors $\left\{\varepsilon_{t}\left[\tau_{\mathrm{D,NU}}^{xy,(\xi)}\left(k_{\mathrm{P}_{\varphi}}\right)\right]\middle|\,\xi=1,2,\cdots,\ S\right\}$ are combined to give the complete uncertainty [i.e. Equation (8) in the main text]:

$$\varepsilon_{\mathrm{total}}\left[\tau_{\mathrm{D,NU}}^{xy}(k)\right] = \sqrt{\frac{\sum_{\xi}\left[\tau_{\mathrm{D,NU}}^{xy,(\xi)}\left(k_{\mathrm{P}_{\varphi}}\right)-\overline{\tau_{\mathrm{D,NU}}^{xy,(\xi)}\left(k_{\mathrm{P}_{\varphi}}\right)}\right]^{2}}{S(S-1)}+\overline{\left\{\varepsilon_{t}\left[\tau_{\mathrm{D,NU}}^{xy,(\xi)}\left(k_{\mathrm{P}_{\varphi}}\right)\right]\right\}^{2}}}, \tag{D13}$$

where $\overline{\tau_{\mathrm{D,NU}}^{xy,(\xi)}\left(k_{\mathrm{P}_{\varphi}}\right)}$ is the final sample estimate (i.e., the mean of the ensemble) for the φ-th time delay. In contrast to the NUACF case, where multiple significant peaks may be analyzed, a single time delay is often sought in NUCCF analysis. In such cases, within a given physically acceptable range, the most frequent (i.e., maximum-likelihood) peak identified across the MC simulations can be selected as the final result.

As argued in Section 2, confidence intervals for the NUCCF should also be derived via MC simulations, because real observation times are fixed and not fully amenable to analytic modeling. The procedure, however, differs from that for the NUACF. To construct the NUCCF confidence interval, we hold one light curve fixed and replace the flux values of the other with a randomly generated white-noise sequence. This process is then repeated with the roles of the two series swapped, yielding two distinct MC-based confidence intervals. A conservative, envelope-based final interval is obtained by taking, at each lag k, the larger absolute bound from the two individual intervals.

Importantly, the construction of confidence intervals for the NUCCF requires consideration of flux measurements, in contrast to the NUACF. Consequently, when estimating time-delay errors via MC simulations, where each run regenerates both light curves based on their flux uncertainties, the NUCCF confidence interval itself must be re-simulated within every individual MC run.

REFERENCES

Alexander, T. 1997, in Astrophysics and Space Science Library, Vol. 218, Astronomical Time Series, ed. D. Maoz, A. Sternberg, & E. M. Leibowitz, 163, doi: 10.1007/978-94-015-8941-3_14

Beutler, F., Blake, C., Colless, M., et al. 2011, MNRAS, 416, 3017, doi: 10.1111/j.1365-2966.2011.19250.x

Billingsley, P. 1995, Probability and Measure, 3rd edn. (Wiley-Interscience)

Bonvin, V., Courbin, F., Suyu, S. H., et al. 2017, MNRAS, 465, 4914, doi: 10.1093/mnras/stw3006

Christy, C. T., Jayasinghe, T., Stanek, K. Z., et al. 2023, MNRAS, 519, 5271, doi: 10.1093/mnras/stac3801

Davis, M., & Peebles, P. J. E. 1983, ApJ, 267, 465, doi: 10.1086/160884

du Mas des Bourboux, H., Le Goff, J.-M., Blomqvist, M., et al. 2017, A&A, 608, A130, doi: 10.1051/0004-6361/201731731

Edelson, R. A., & Krolik, J. H. 1988, ApJ, 333, 646, doi: 10.1086/166773

Eisenstein, D. J., Zehavi, I., Hogg, D. W., et al. 2005, ApJ, 633, 560, doi: 10.1086/466512

Fei, Y., Yu, C., Li, K., et al. 2024, ApJS, 275, 10, doi: 10.3847/1538-4365/ad785b

Franks, L. E. 1981, Signal Theory, revised edn. (Dowden & Culver, Inc.)

Freedman, W. L., Madore, B. F., Gibson, B. K., et al. 2001, ApJ, 553, 47, doi: 10.1086/320638

Gaia Collaboration, Vallenari, A., Brown, A. G. A., et al. 2023, A&A, 674, A1, doi: 10.1051/0004-6361/202243940

Hernández Santisteban, J. V., Edelson, R., Horne, K., et al. 2020a, MNRAS, 498, 5399, doi: 10.1093/mnras/staa2365

Hernández Santisteban, J. V., Edelson, R., Horne, K., et al. 2020b, Intensive disc-reverberation mapping of Fairall 9: 1st year of Swift & LCO monitoring, 1.0, Zenodo, doi: 10.5281/zenodo.3956577

Jokipii, J. R. 1966, ApJ, 146, 480, doi: 10.1086/148912

Kamionkowski, M., Kosowsky, A., & Stebbins, A. 1997, PhRvD, 55, 7368, doi: 10.1103/PhysRevD.55.7368

Kauffmann, G., Colberg, J. M., Diaferio, A., & White, S. D. M. 1999, MNRAS, 303, 188, doi: 10.1046/j.1365-8711.1999.02202.x

Kelly, B. C., Bechtold, J., & Siemiginowska, A. 2009, ApJ, 698, 895, doi: 10.1088/0004-637X/698/1/895

King, J. H., & Papitashvili, N. E. 2005, Journal of Geophysical Research (Space Physics), 110, A02104, doi: 10.1029/2004JA010649

Kreutzer, L. T., Gillen, E., Briegal, J. T., & Queloz, D. 2023, MNRAS, 522, 5049, doi: 10.1093/mnras/stad1223

Landy, S. D., & Szalay, A. S. 1993, ApJ, 412, 64, doi: 10.1086/172900

Li, X., Niu, C., Zhang, J., et al. 2026, arXiv e-prints, arXiv:2603.07123, doi: 10.48550/arXiv.2603.07123

Lomb, N. R. 1976, Ap&SS, 39, 447, doi: 10.1007/BF00648343

Lyubarskii, Y. E. 1997, MNRAS, 292, 679, doi: 10.1093/mnras/292.3.679

Masci, F. J., Laher, R. R., Rusholme, B., et al. 2019, PASP, 131, 018003, doi: 10.1088/1538-3873/aae8ac

McQuillan, A., Aigrain, S., & Mazeh, T. 2013, MNRAS, 432, 1203, doi: 10.1093/mnras/stt536

Mo, H. J., & White, S. D. M. 1996, MNRAS, 282, 347, doi: 10.1093/mnras/282.2.347

Mosser, B., & Appourchaux, T. 2009, A&A, 508, 877, doi: 10.1051/0004-6361/200912944

Nimmo, K., Pleunis, Z., Beniamini, P., et al. 2025, Nature, 637, 48, doi: 10.1038/s41586-024-08297-w

Pal, A. 2025, ApJL, 983, L15, doi: 10.3847/2041-8213/adc386

Pal, M., Dewangan, G. C., Connolly, S. D., & Misra, R. 2017, MNRAS, 466, 1777, doi: 10.1093/mnras/stw3173

Pancoast, A., Brewer, B. J., & Treu, T. 2014, MNRAS, 445, 3055, doi: 10.1093/mnras/stu1809

Peebles, P. J. E. 1980, The large-scale structure of the universe

Peterson, B. M., Ferrarese, L., Gilbert, K. M., et al. 2004, ApJ, 613, 682, doi: 10.1086/423269

Press, W. H., Rybicki, G. B., & Hewitt, J. N. 1992, ApJ, 385, 404, doi: 10.1086/170951

Riess, A. G., Yuan, W., Macri, L. M., et al. 2022, ApJL, 934, L7, doi: 10.3847/2041-8213/ac5c5b

Scargle, J. D. 1982, ApJ, 263, 835, doi: 10.1086/160554

Springel, V., Pakmor, R., Pillepich, A., et al. 2018, MNRAS, 475, 676, doi: 10.1093/mnras/stx3304

Starkey, D., Horne, K., Fausnaugh, M. M., et al. 2017, ApJ, 835, 65, doi: 10.3847/1538-4357/835/1/65

Starkey, D. A., Horne, K., & Villforth, C. 2016, MNRAS, 456, 1960, doi: 10.1093/mnras/stv2744

Sun, M., Grier, C. J., & Peterson, B. M. 2018, PyCCF: Python Cross Correlation Function for reverberation mapping studies, Astrophysics Source Code Library, record ascl:1805.032. http://ascl.net/1805.032

Tewes, M., Courbin, F., & Meylan, G. 2013, A&A, 553, A120, doi: 10.1051/0004-6361/201220123

Timmer, J., & König, M. 1995, A&A, 300, 707

VanderPlas, J. T. 2018, ApJS, 236, 16, doi: 10.3847/1538-4365/aab766

Wong, K. C., Suyu, S. H., Chen, G. C.-F., et al. 2020, MNRAS, 498, 1420, doi: 10.1093/mnras/stz3094

Yang, Y.-P., & Zhang, B. 2023, MNRAS, 522, 4907, doi: 10.1093/mnras/stad1311

Yu, C. 2024, An Expandable Light Curve Dataset for Automatic Classification of Variable Stars (LEAVES), National Astronomical Data Center, DR1, doi: 10.12149/100962